



CO₂- and orbitally- driven oxygen isotope variability in the Early Eocene

Julia Campbell¹, Christopher J. Poulsen^{1,2}, Jiang Zhu³, Jessica E. Tierney⁴, and Jeremy Keeler¹

¹Department of Earth and Environmental Sciences, University of Michigan, Ann Arbor, 48104, USA

5 ²Department of Earth Sciences, University of Oregon, Eugene, 97403, USA

³Climate and Global Dynamics Laboratory, National Center for Atmospheric Research, Boulder, 80301, USA

⁴Department of Geosciences, University of Arizona, Tucson, 85721, USA

Correspondence to: Julia Campbell (juliacam@umich.edu)

Abstract. Paleoclimate reconstructions of the Early Eocene provide important data constraints on the climate and hydrologic
10 cycle under extreme warm conditions. Available terrestrial water isotope records have been primarily interpreted to signal an
enhanced hydrologic cycle in the Early Eocene associated with large-scale warming induced by high atmospheric CO₂.
However, orbital-scale variations in these isotope records have been difficult to quantify and largely overlooked, even
though orbitally driven changes in solar irradiance can impact temperature and the hydrologic cycle. In this study, we fill this
gap using water isotope-climate simulations to investigate the orbital sensitivity of Earth's hydrologic cycle under different
15 CO₂ background states. We analyze the relative difference between climatic changes resulting from CO₂ and orbital changes
and find that the seasonal climate responses to orbital changes are larger than CO₂-driven changes in several regions. Using
terrestrial δ¹⁸O and δD records from the Paleocene-Eocene Thermal Maximum (PETM), we compare our modeled isotopic
seasonal range to fossil evidence and find agreement between empirical and simulated isotopic compositions. Our
conclusions consider systematic impacts on the proxy records, including the preservation state of the proxy, analytical
20 uncertainty, and the relationship between δ¹⁸O or δD and environmental context, as well as illustrate the utility of fully
coupled, isotope-enabled climate models when interpreting proxy records in times of extreme warmth.

1 Introduction

25 The Earth has rapidly warmed since the preindustrial (PI) era, driving substantial and widespread changes in the hydrologic
cycle (Douville et al., 2021). Severe warming and changes in the water cycle are projected to continue depending on the
level of greenhouse gas emissions. Following a higher emissions pathway, atmospheric CO₂ will exceed 1,000 ppm by the
end of the 21st century, a level that last existed during the Early Eocene about 56-48 million years ago (Tierney et al., 2020).
Understanding the temperature and water cycle of the most recent extreme warmth may help us to better understand what
30 lies ahead.



35 The Early Eocene likely experienced atmospheric CO₂ concentrations at 3x PI levels (Rae et al., 2021). The Paleocene-Eocene Thermal Maximum (PETM) was a ~100,000-year time interval within the Early Eocene that experienced especially rapid warming with global surface temperatures rising 5-6°C in response to an increase in CO₂ levels as high as 6x PI CO₂ (Zhu et al., 2019; Tierney et al., 2022). Simulation of this warming event furthers our understanding of how the Earth operates under a high CO₂ background state. There is still much to learn about the Early Eocene and the PETM, especially surrounding the relative influence changes in orbit have on the hydrologic cycle.

40 Earth's orbital configuration has a strong influence on regional climate and is a driver of major climatic fluctuations such as the ice ages (Berger, 1988). The orbit determines the timing and intensity of sunlight for a given region and season. Obliquity, the tilt on Earth's axis, has a ~41,000-year cycle; precession, the Earth's wobble, is a ~22,000-year cycle; and eccentricity, the Earth's path around the sun, lasts ~100,000 years. These three factors together determine the solar irradiance any area on Earth will receive at a given time, including the ice sheets which dramatically influence global climate (Ruddiman, 2006). A higher eccentricity and a higher obliquity cause heightened seasonality, including warmer summer 45 seasons (Berger, 1988). Seasonal shifts in solar insolation also drive temperature changes which impact the isotopes of precipitation, and therefore the proxy records related to the isotopic composition of precipitation.

50 There is evidence of orbital-scale variations in atmospheric CO₂ during the Late Paleocene and Early Eocene (Zeebe et al., 2017). Orbitally induced changes in the oceanic temperatures and circulation may have also been a cause for the frequent and variable hyperthermals during the Early Eocene (Lunt et al., 2011). The PETM was the most extreme hyperthermal, a consequence of even greater atmospheric CO₂ concentrations and potentially greater seasonal changes owing to the Earth's orbit. By modeling different orbital and CO₂ configurations and matching the simulations to fossil evidence, we can provide context for the proxy records and learn how the orbit may have played a part in the severe warming at the onset of the PETM, as well as different seasonal impacts on the Early Eocene climate.

55 Oxygen and hydrogen isotopic ratios from meteoric waters are often used as a measure of climate variability, including variability by changing CO₂ concentrations or orbit. The ratio of heavy (¹⁸O, ²H) to light (¹⁶O, ¹H) isotopes is represented by δ¹⁸O or δD (Craig, 1961). Warmer global temperatures mean more energy in the troposphere to increase evaporation of the heavier isotope – commonly referred to as the temperature effect, and decreased precipitation results in rainfall more 60 enriched in the heavier isotope – commonly referred to as the amount effect, which increases the atmospheric δ¹⁸O or δD (Craig, 1961). This can be linked to orbit and atmospheric CO₂ because distribution of solar insolation and greenhouse gas concentrations each drive global temperature and precipitation trends, which then influence the δ¹⁸O or δD of precipitation (δ¹⁸O_p, δD_p) (Craig, 1961). Although the Early Eocene and PETM have been modeled before, these are the first simulations of that time period to reproduce the extreme warmth and weakened meridional temperature gradient of the PETM, as well as



65 track water isotopes through the hydrologic cycle – which can offer more information on evaporation, advection,
precipitation, and other factors that influence $\delta^{18}\text{O}_p$ and δD_p (Zhu et al., 2020).

In this study, we investigate the Early Eocene’s climatic and hydrologic response to changes in Earth’s orbit and atmospheric
CO₂ concentration in order to further understand the impact of orbit on the hydrologic cycle during warm climates and to test
70 Earth’s sensitivity to changes in orbit under different CO₂ background states. Additionally, we include comparisons between
these responses and terrestrial $\delta^{18}\text{O}$ and δD records to test the model’s ability to simulate changes in the hydrologic cycle in
an extremely warm climate. These analyses strengthen our comprehension of the environmental context of terrestrial proxy
records, the potential of orbital changes to partly initiate the hyperthermal, the influence of orbit on the hydrologic cycle at
different CO₂ forcings, and the potential of this model to simulate climate changes during a time with a higher atmospheric
75 CO₂ level than today.

2 Methodology

2.1 Earth system modeling

The Eocene simulations used here were previously described in Tierney et al (2022) where they were used for a paleoclimate
80 data assimilation reconstruction of PETM climate. The simulations were conducted using a water isotope-enabled
Community Earth System Model (iCESM) version 1.2. CESM1.2 is comprised of the Community Atmosphere Model
(CAM) version 5.3, Community Land Model (CLM) version 4.0, Community Ice Code (CICE) version 4.0, River Transport
Model (RTM), Parallel Ocean Program (POP) version 2, and a coupler to connect them (Hurrell et al., 2013). In addition,
iCESM has the capability to simulate the transport and transformation of water isotopes in the model hydrologic cycle
85 (Brady et al., 2019). The model resolution is 1.9° x 2.5° for the atmosphere and land, and a nominal 1° for ocean and sea ice.
The paleogeography, land-sea mask, and vegetation distribution follow the Deep-Time Modeling Intercomparison Project
(DeepMIP) protocol at about 55 million years ago (Herold et al., 2014). The ocean temperature and salinity were initialized
from a PETM quasi-equilibrated state, and the $\delta^{18}\text{O}$ of seawater was initialized from a constant -1‰ to account for the
absence of ice sheets in a hothouse climate (Zhu et al., 2020). There are four orbital configurations, each modeled at both a
90 low (3x PI) and high (6x PI) CO₂ concentration, including a modern orbit (OrbMod), maximum summer solar insolation for
the Southern Hemisphere (OrbMaxS), maximum summer solar insolation for the Northern Hemisphere (OrbMaxN), and
minimum eccentricity (OrbMin) (Lunt et al., 2011). The OrbMaxS and OrbMaxN simulations experience high eccentricity
and obliquity, so those simulations would expect high seasonality (Lunt et al., 2011). A control simulation was run for 2000
model years. Orbital cases were branched from the control simulation and run for an additional 500 model years each. The
95 climatological means presented in the results are based on the last 100 years of each simulation. Mean annual climatologies
can be found in Figs. A11-A13. All simulations had an atmospheric CH₄ concentration of 791.6 ppb and an atmospheric N₂O



concentration of 275.68 ppb. CO₂ and orbital details for the modeled cases discussed here are available in Table 1. Further details are available in Tierney et al (2022).

	3x PI OrbMod	3x PI OrbMin	3x PI OrbMaxN	3x PI OrbMaxS	6x PI OrbMod	6x PI OrbMin	6x PI OrbMaxN	6x PI OrbMaxS
CO ₂ (ppm)	854.1	854.1	854.1	854.1	1708.2	1708.2	1708.2	1708.2
Eccentricity	0.0167	0.0	0.054	0.054	0.0167	0.0	0.054	0.054
Obliquity	23.45	22	24.5	24.5	23.45	22	24.5	24.5
Moving Vernal Equinox Longitude of Perihelion	90	0	270	90	90	0	270	90

100

Table 1: The atmospheric CO₂ concentrations and orbital details are presented here for each modeled case. OrbMod represents a modern orbit, OrbMin represents a minimum eccentricity orbit with mild seasons, and OrbMaxN and OrbMaxS represent maximum eccentricity orbits with heightened seasonality. The longitude of the perihelion is the angle between the Earth at the Northern Hemisphere (NH) autumnal equinox and the Earth at its closest to the sun – 0° represents a perihelion at the NH autumnal equinox, 90° is at the NH winter solstice, 180° is at the NH vernal equinox, and 270° is at the NH summer solstice. For example, the NH is closest to the sun during the NH summer solstice in OrbMaxN (Fig. A1).

105

2.2 Proxy records

110

There are more hydrological isotope proxy data from the PETM, so that time interval is the focus here, rather than the Early Eocene. The 6x PI CO₂ simulations are compared to several terrestrial proxy records of δ¹⁸O and δD from the PETM (Table 2). Our focus is on terrestrial proxies over marine proxies as terrestrial proxies are more heavily impacted by changing orbit and seasonality, given the land-ocean warming contrast (Byrne and O’Gorman, 2013). There is strong model-data agreement with terrestrial temperature proxies which validates the Early Eocene (3x PI CO₂) simulations (Fig. A2, Zhu et al., 2019).

115

These Eocene simulations also show strong agreement with marine proxies, as discussed in Zhu et al (2020).

120

Paleosol carbonates and siderite preserve the soil water they form in, so an isotopic comparison with simulated soil water, rather than precipitation, is the most salient comparison. However, rainfall is the main source for water at the depth that these soil carbonates form, so the soil water isotopic signals are very similar to the precipitation isotopic signals. Soil carbonates are likely to form around 40-100 cm deep, so the simulated δ¹⁸O range represents soil water at this depth as well (Burgener et al., 2016). In order to compare the proxy δ¹⁸O to simulated soil water δ¹⁸O, a proxy system model (PSM) is needed to transform δ¹⁸O of the soil carbonate to δ¹⁸O of the water in which they precipitated from. The fractionation factor is controlled by the local soil temperature, so each location has a slightly different fractionation factor, though all are near 1



(van Dijk et al., 2018; Friedman and O’Neil, 1977). The siderite’s oxygen fractionation was calculated through Van Dijk’s
 125 best fit equation (van Dijk et al., 2018). The paleosol carbonate’s oxygen fractionation was calculated through the USGS
 equation (Friedman and O’Neil, 1977).

Leaf waxes are another powerful tool for paleoclimate reconstruction but also require a PSM to account for the
 transformations between the δD of soil water and the δD within the leaf wax (Konecky et al., 2019). Therefore, the δD
 130 model-data comparison includes δD from PETM leaf waxes and model-inferred leaf wax δD seasonal ranges. Comparing
 leaf wax δD in addition to the soil $\delta^{18}O$ proxies offers an opportunity to explore hydrogen isotope accuracy within iCESM.
 The model-inferred leaf wax δD values were calculated through the WaxPSM using the zonal seasonal range of soil water
 δD and a global, fixed apparent fractionation factor of -124‰ (Konecky et al., 2019). The apparent fractionation factor
 differs between different plants, but it is unknown for Early Eocene vegetation, so this study uses an average value for a
 135 modern landscape that is equal parts shrubs, trees, forbs, and C3 grasses (Sachse et al., 2012).

Author (Year)	Sample Type	Age
Bataille et al (2016)	Paleosol Carbonate, $\delta^{18}O$	PETM
Bowen et al (2015)	Paleosol Carbonate, $\delta^{18}O$	PETM
Kelson et al (2018)	Paleosol Carbonate, $\delta^{18}O$	PETM
Koch et al (1995)	Paleosol Carbonate, $\delta^{18}O$	PETM
Snell et al (2013)	Paleosol Carbonate, $\delta^{18}O$	PETM
White et al (2017)	Siderite, $\delta^{18}O$	PETM
Van Dijk et al (2020)	Siderite, $\delta^{18}O$	PETM
Pagani et al (2006)	Leaf Wax, δD	PETM
Handley et al (2008)	Leaf Wax, δD	PETM
Handley et al (2011)	Leaf Wax, δD	PETM
Smith et al (2007)	Leaf Wax, δD	PETM
Tipple et al (2011)	Leaf Wax, δD	PETM
Garel et al (2013)	Leaf Wax, δD	PETM
Jaramillo et al (2010)	Leaf Wax, δD	PETM
Huber and Caballero (2011)	Macroflora, Temperature	Early Eocene

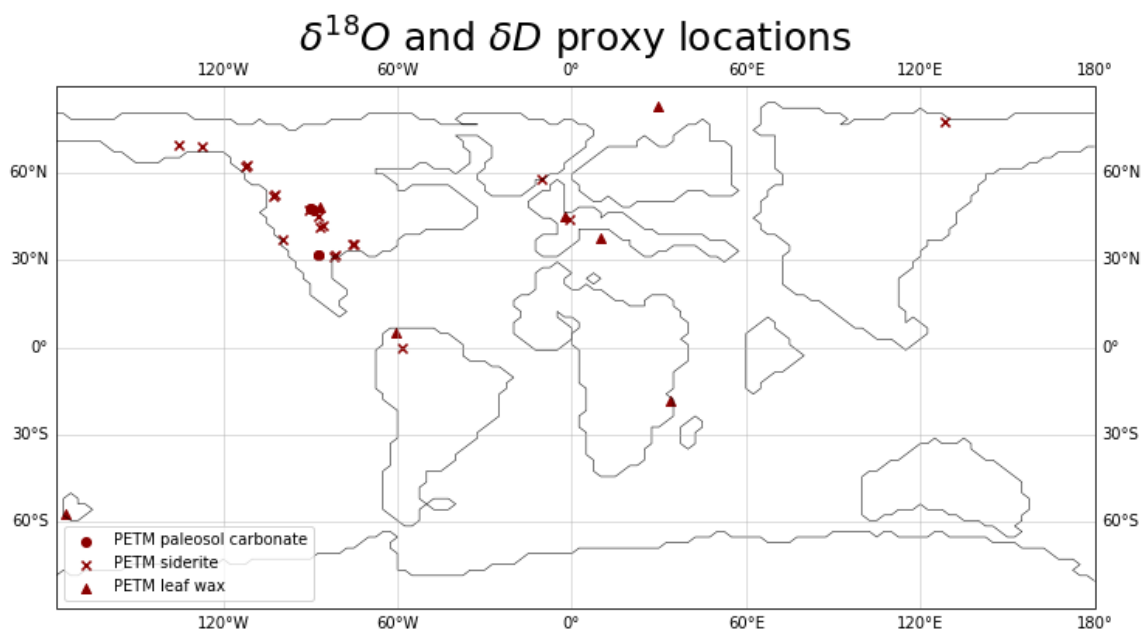


140

Table 2: A list of the proxy records used in model-data comparisons. Paleosol carbonates and siderite are used for a PETM oxygen isotope comparison, and leaf fossils are used for a PETM hydrogen isotope comparison. A terrestrial temperature comparison, reconstructed from macroflora fossil evidence, is used to validate the Early Eocene (3x PI CO₂) simulations in Fig. A2.

145

The soil carbonate proxies act as a time-integrated record of environmental changes over hundreds to thousands of years and are not tied to specific orbital configurations (Burgener et al., 2016). Although the proxy records span a wide geographic range, we could not find published terrestrial $\delta^{18}\text{O}$ proxy records for the PETM from the Southern Hemisphere (SH), which signals a need for more focus and funding to be directed to researchers in the SH to fill this gap. The locations of the proxies were converted to paleo-coordinates suitable for our paleogeographic reconstruction (Fig. 1, Muller et al., 2018).



150

Figure 1: The Early Eocene paleogeography used for the model simulations, with points overlaid representing the locations of the PETM terrestrial isotope proxy record. Note that two of the records originated on islands that don't appear on this paleogeographic map. There is a noticeable lack of paleo-isotope records from the SH.

3 Results

155

3.1 Response to orbit

High eccentricity and obliquity cause more intense seasonality (Berger, 1988). We focus our analysis on the OrbMaxS and OrbMaxN simulations because their large seasonal insolation variations drive the greatest terrestrial climate response (Fig. A1). OrbMaxS and OrbMaxN are also at the same (high) eccentricity and obliquity as one another, so these differences are



160 results of precessional changes only (Table 1). Sect. 3.1 focuses on response to orbit at the 3x PI CO₂ level because there were greater climatic differences between orbits at this level (see Sect. 3.3).

The seasonal surface temperature differences between OrbMaxS and OrbMaxN are driven by the changes in insolation between the two orbits (Figs. 2, A3). Differential solar heating, controlled by orbital forcing, gives rise to a latitudinal temperature gradient and has a great influence on Earth's climate (Davis and Brewer, 2011). Insolation changes also drive differences in specific humidity between these runs, since warmer air can hold more water vapor with an increase in saturation vapor pressure (SVP) (Fig. A4). However, areas that experience an increase in temperature and specific humidity largely experience a decrease in relative humidity, the ratio of water vapor to the SVP, as SVP increases more than specific humidity during warming (Fig. A5, Tichy et al., 2017). Lower relative humidity results in a lower chance of cloud formation and rainfall, which often only occurs when relative humidity is >90%.

Regions like northern Africa or the Tibetan Plateau experience increases in temperature and decreases in precipitation, as well as increases in $\delta^{18}\text{O}_p$ due to temperature and amount effects (Figs. 2, 3 4). Changes in insolation distribution shift the position of the inter-tropical convergence zone (ITCZ) toward the hemisphere receiving the greatest insolation. As a result, in the OrbMaxS (OrbMaxN) simulation, there are slightly wetter conditions in the SH (NH) than in the NH (SH) (Figs. 3, 6). In the hemisphere with greater precipitation, meteoric water is generally more ¹⁸O-depleted (Fig. 4). Globally, the large-scale simulated δD_p patterns mimic the large-scale simulated $\delta^{18}\text{O}_p$ patterns, since the fractionation of hydrogen and oxygen are controlled by the same distillation factors (Fig. A6). Both $\delta^{18}\text{O}_p$ and δD_p exhibit large-scale seasonal differences between OrbMaxS and OrbMaxN; DJF (JJA) experiences greater (lesser) $\delta^{18}\text{O}_p$ and δD_p in OrbMaxS than OrbMaxN driven by the difference in seasonal insolation (Figs. 4, A6).

Aside from the large-scale isotopic signals, specific regions experience large seasonal differences in $\delta^{18}\text{O}_p$ with a change in orbit. For instance, western North America sees a substantial ¹⁸O-depletion in precipitation during JJA when comparing OrbMaxS to OrbMaxN, up to -5‰ (Fig. 4). JJA is the SH winter season, so most of the Earth is colder at this time in the OrbMaxS simulations, especially regions of high elevation like the North American Cordillera, which likely had an elevation upwards of 3 km in some areas (Mulch et al., 2007). The decrease in temperature resulted in an increase in relative humidity in the area, increasing cloud cover and rainfall (Figs. 3, A5). Mountains already intensify vapor fractionation, reducing the $\delta^{18}\text{O}_p$ through the amount and temperature effects, so the Cordillera experienced especially depleted rainfall during JJA for the OrbMaxS simulations compared to the OrbMaxN simulations, which experienced a very hot NH during JJA (Fig. 4, Poulsen et al., 2007). Furthermore, northern Africa experiences enriched rainfall during all seasons, especially SON, with differences up to 6.5‰ between OrbMaxS and OrbMaxN (Fig. 4). Temperatures are warmer year-round, and relative humidity and rainfall rates are lower, resulting in substantially enriched rainfall. In addition to that, moisture transport likely



195

has an influential role on increasing $\delta^{18}\text{O}_p$ in this area due to relatively deep atmospheric convection in the Indo-Pacific warm pool (Konecky et al., 2019).

Seasonal temperature differences (OrbMaxS - OrbMaxN) at 3x PI CO_2

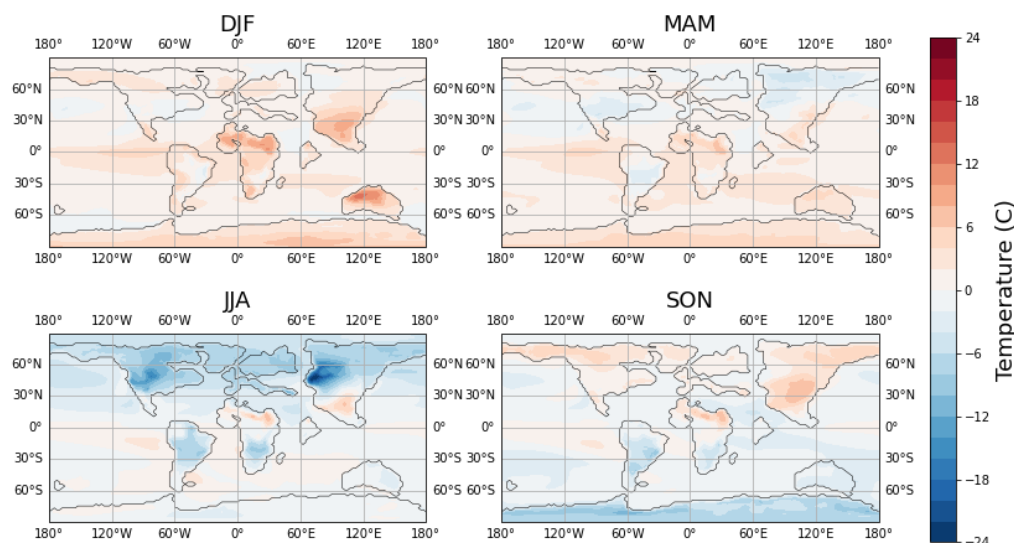
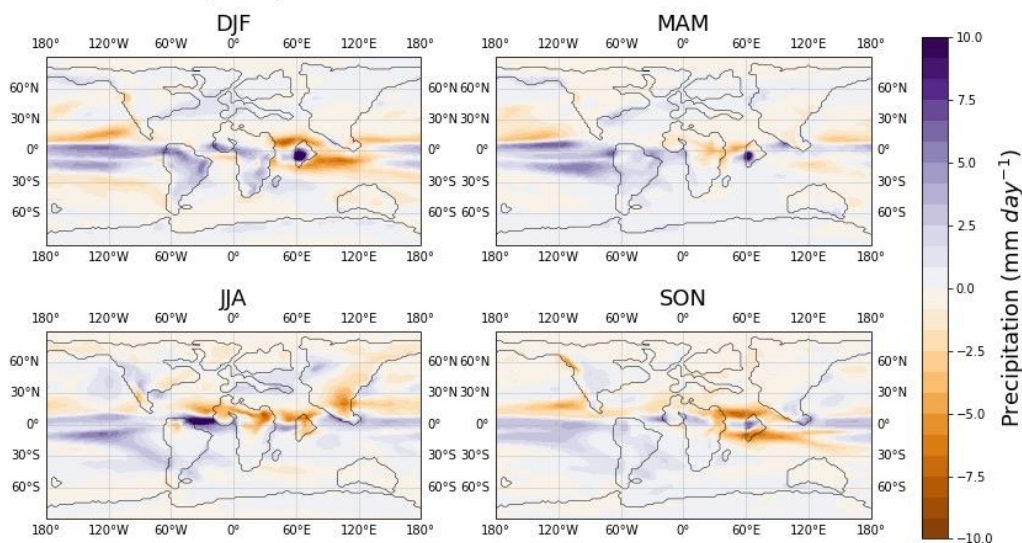


Figure 2: The seasonal temperature differences between OrbMaxS and OrbMaxN at 3x PI CO_2 .

Seasonal precipitation differences (OrbMaxS - OrbMaxN) at 3x PI CO_2



200 Figure 3: The seasonal precipitation differences between OrbMaxS and OrbMaxN at 3x PI CO_2 . The maximum positive precipitation difference on the corresponding color bar represents anything experiencing 10 mm day^{-1} or higher.

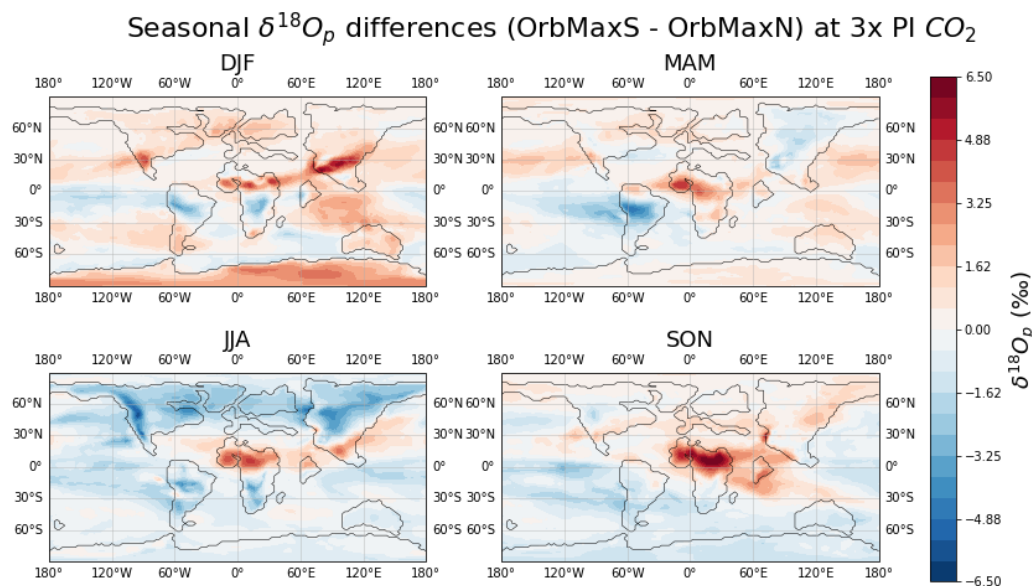


Figure 4: The seasonal $\delta^{18}\text{O}_p$ differences between OrbMaxS and OrbMaxN at 3x PI CO_2 .

205

3.2 Response to CO_2

With constant orbital parameters, simulated climate responds strongly to changes in atmospheric CO_2 levels as well. Increasing greenhouse gases results in warmer global temperatures, an enhanced hydrologic cycle, and ^{18}O enrichment over land (Figs. 5, 7). Sect. 3.2 shows hydrological and $\delta^{18}\text{O}_p$ responses to increased CO_2 for both OrbMaxS and OrbMaxN. Seasonal partitioning did not reveal any further insights, so the following results are averaged annually.

As a consequence of the greenhouse effect, global surface temperatures increase by as much as $\sim 13^\circ\text{C}$ in the 6x PI CO_2 simulations compared to the 3x PI CO_2 simulations (Fig. 5). There is also an increase in downward shortwave radiation owing to a 4-5% reduction in total cloud cover in the 6x PI CO_2 simulations (Fig. A7). There is a greater rise in temperature over land than ocean – an average 41-44% increase in surface temperature over land compared to an average 17-19% increase in surface temperature over ocean, largely owing to the land-sea contrast in heat capacities (Fig. 5, Dong et al., 2009). The increased temperatures produce higher rates of evaporation for the heavier oxygen isotope and increases the residence time of water vapor in the atmosphere, which may contribute to an increased advective length scale of enriched moisture transport (Singh et al., 2016). The decreased relative humidity leads to decreased rates of precipitation, which result in increased $\delta^{18}\text{O}_p$ over most of the globe in the 6x PI CO_2 simulations (Figs. 6, 7, A8).

Though most areas exhibit an increase in $\delta^{18}\text{O}_p$ with the 6x PI CO_2 modeled case, the western equatorial Pacific and some subpolar regions show a slight decrease (Fig. 7). These regions experience increases in relative humidity, cloud cover, and



225 precipitation under the higher CO₂ background state, resulting in ¹⁸O-depleted rainfall (Figs. 6, A7, A8). The colder subpolar region does not experience much of an increase in surface air temperatures, which may have contributed to the slight increase in relative humidity (Fig. 5). The equatorial Pacific sees an increase in temperature, but it also experiences highly increased rainfall (Fig. 6). There has been previous evidence of a narrowing and strengthening of the ITCZ during the onset of the PETM, which would increase precipitation, resulting in decreased $\delta^{18}\text{O}_p$ (Tierney et al., 2022).

230 The North American Cordillera experiences large increases in $\delta^{18}\text{O}_p$ under the higher CO₂ conditions (Fig. 7). Areas of high elevation generally have very low $\delta^{18}\text{O}_p$ compared to areas of low elevation due to isotopic distillation during rainout. This elevation distinction is reduced during times of extremely warm temperatures due to atmospheric subsidence of vapor enriched in ¹⁸O, which explains the substantial increase, up to 3‰, in $\delta^{18}\text{O}_p$ with a doubled CO₂ (Fig. 7, Poulsen and Jeffery, 2011). However, OrbMaxN does not see as dramatic an increase in $\delta^{18}\text{O}_p$ under higher CO₂ conditions at this mountain range (Fig. 7). The isotopic response is lower because the higher insolation in the NH at OrbMaxN already caused a response under the 3x PI CO₂ conditions. $\delta^{18}\text{O}_p$ over the mountain range is higher in the OrbMaxN case than the other cases at 3x PI CO₂ because the increased insolation warmed the mountain range and increased $\delta^{18}\text{O}_p$ substantially, so there is a smaller difference in $\delta^{18}\text{O}_p$ between the CO₂ levels (Fig. 7).

240 Finally, most orbits display just a slight increase in $\delta^{18}\text{O}_p$ in northern Africa under the higher CO₂ state, but OrbMaxN experiences a substantial increase in $\delta^{18}\text{O}_p$ in northern Africa, up to 3‰, largely owing to drier conditions (Figs. 6, 7, A8). Northern Africa experiences a stronger decrease in relative humidity for OrbMaxN than any other orbit under the higher CO₂ state (Fig. A8). The decrease in relative humidity and precipitation results in more enriched rainfall, causing a stronger increase in $\delta^{18}\text{O}_p$ over this desert and shrubland region under OrbMaxN conditions.

245

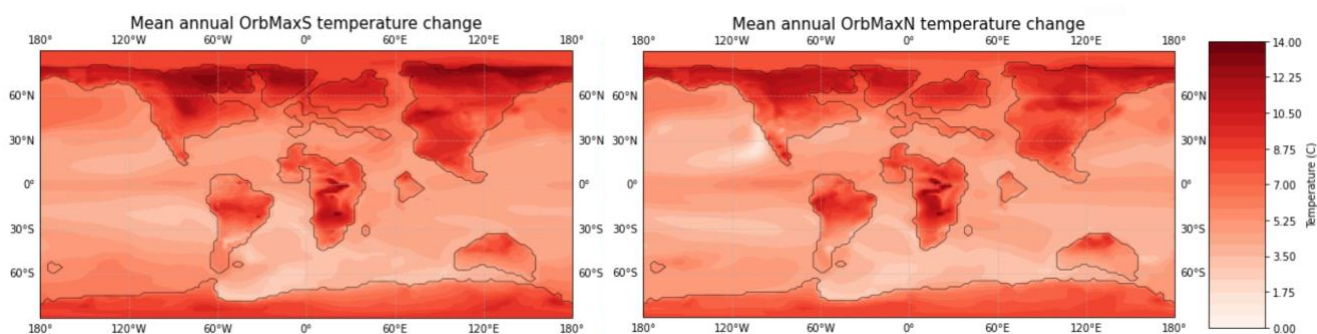


Figure 5: The difference in mean annual surface temperatures at 6x PI CO₂ compared to 3x PI CO₂ for OrbMaxS (left) and OrbMaxN (right). To view absolute mean annual surface air temperatures, see Fig. A11.

250

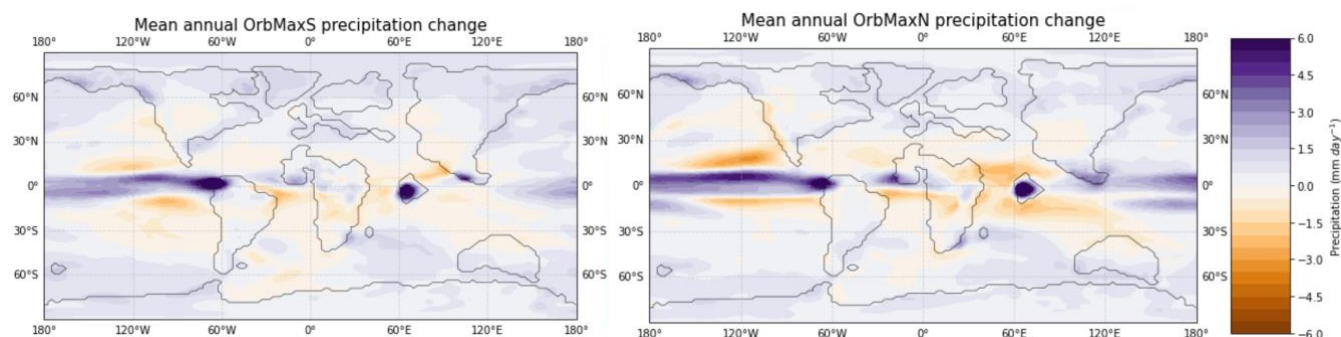


Figure 6: The difference in mean annual precipitation under 6x PI CO₂ compared to 3x PI CO₂ for OrbMaxS (left) and OrbMaxN (right). The maximum positive precipitation difference on the corresponding color bar represents anything experiencing 6.0 mm day⁻¹ or higher. To view absolute mean annual precipitation, see Fig. A12.

255

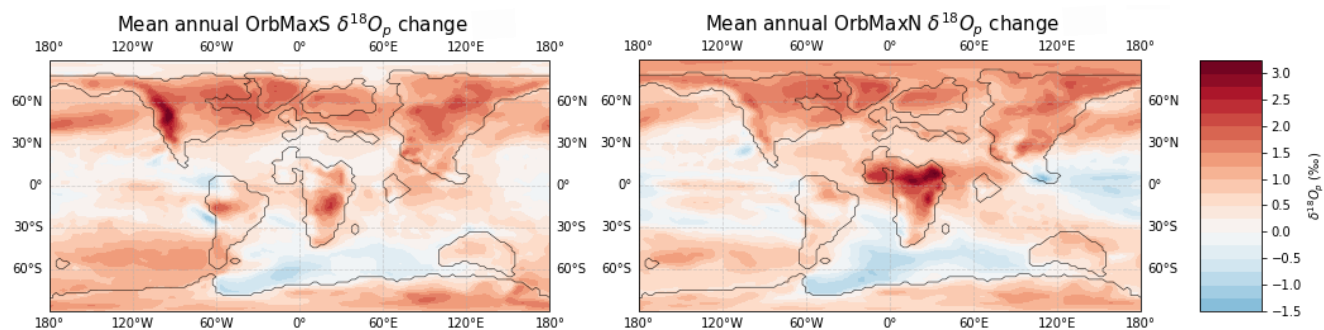


Figure 7: The difference in mean annual $\delta^{18}\text{O}_p$ at 6x PI CO₂ compared to 3x PI CO₂ for OrbMaxS (left) and OrbMaxN (right). To view absolute mean annual $\delta^{18}\text{O}_p$, see Fig. A13.

260 3.3 Orbital sensitivity under different CO₂ background states

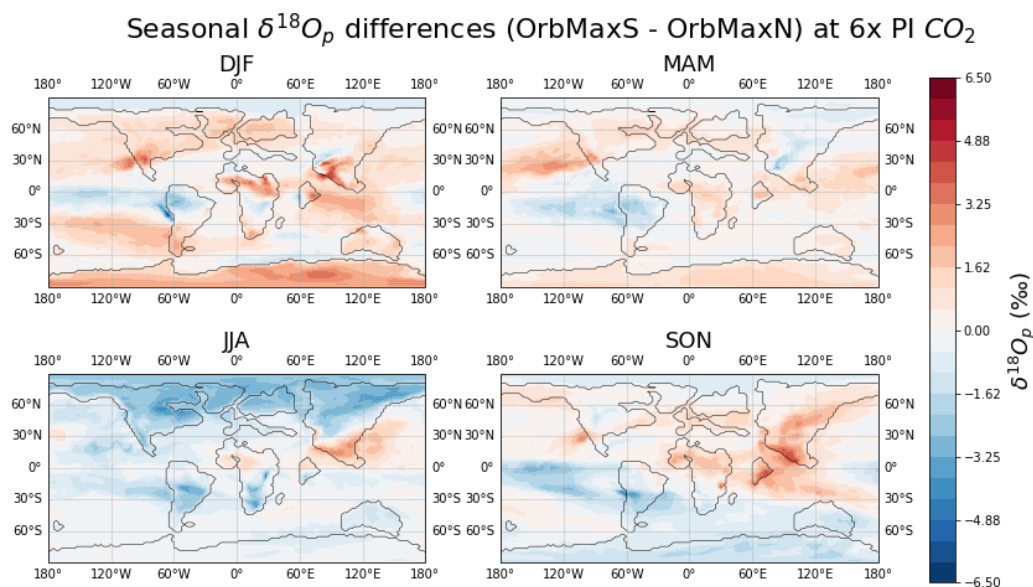
Given the above results, the hydrologic cycle is clearly impacted by both changes in orbit and changes in atmospheric CO₂ levels. However, none of the above results address the potential difference in the hydrologic cycle's orbital sensitivity under two different CO₂ background states. In other words, do changes in orbit at a lower CO₂ level have a greater impact on the oxygen isotopic ratio of precipitation than changes in orbit at a higher CO₂ level? When comparing the $\delta^{18}\text{O}_p$ differences between OrbMaxS and OrbMaxN at 3x PI CO₂ versus 6x PI CO₂, the spatial patterns of enrichment and depletion of heavy oxygen isotopes are similar (Figs. 4, 8). However, the global mean annual $\delta^{18}\text{O}_p$ difference between these two orbits is over 20% smaller for 6x PI CO₂ than 3x PI CO₂. Averaged globally, the change in orbit has a smaller impact on the hydrologic cycle at the higher CO₂ level, representative of the PETM.

270

Additionally, the regions that experience a larger enrichment or depletion of heavy oxygen isotopes between orbits during certain seasons, like western North America or northern Africa, see a much smaller $\delta^{18}\text{O}_p$ difference at the higher CO₂ level than the lower CO₂ level, by as much as 4‰ (Figs. 4, 8). Therefore, the higher atmospheric CO₂ level dampens the orbital



275 sensitivity of the hydrologic cycle, especially in these regions. Fractionation of oxygen isotopes is more pronounced at lower
temperatures, and the 3x PI CO₂ background state exhibits much lower global temperatures than the 6x PI CO₂ background
state (Fig. 5, Luz et al., 2009). CO₂-induced warming tends to slow general circulation in the tropics and subtropics (Singh et
al., 2016). Higher temperatures result in higher rates of evaporation, an increase in water vapor residence time, and more ¹⁸O
in the atmosphere, which causes a lower fractionation factor between the lighter and heavier oxygen isotopes and less rainout
and distillation (Luz et al., 2009). The smaller fractionation rate between oxygen isotopes during evaporation and decrease in
280 rainout and distillation results in smaller, muted differences in the oxygen isotope variability of precipitation between orbits.
Therefore, the change in insolation distribution has less of a considerable impact on the hydrologic cycle at higher
atmospheric CO₂ levels.



285 **Figure 8: The seasonal $\delta^{18}O_p$ differences between OrbMaxS and OrbMaxN at 6x PI CO₂.**

3.4 Model-data comparison

290 Isotope-enabled climate models can simulate the transformation and transportation of water isotopes in all components of the
model, which allows for direct comparison between modeled isotopic ratios and paleo-recorded isotopic ratios, and further
assessment of uncertainties (Zhu et al., 2017). This study gathers $\delta^{18}O$ data from soil carbonates and δD data from leaf
waxes in order to validate iCESM's simulated terrestrial hydrologic cycle during the PETM, which had more available data
than the Early Eocene. The lower CO₂ background state, representative of the greater Early Eocene age, is validated through
a terrestrial temperature model-data comparison (Fig. A2, Zhu et al., 2019). The isotopic model-data comparison results
295 focus only on the 6x PI CO₂ simulations and PETM records. The comparisons account for seasonality by including both the

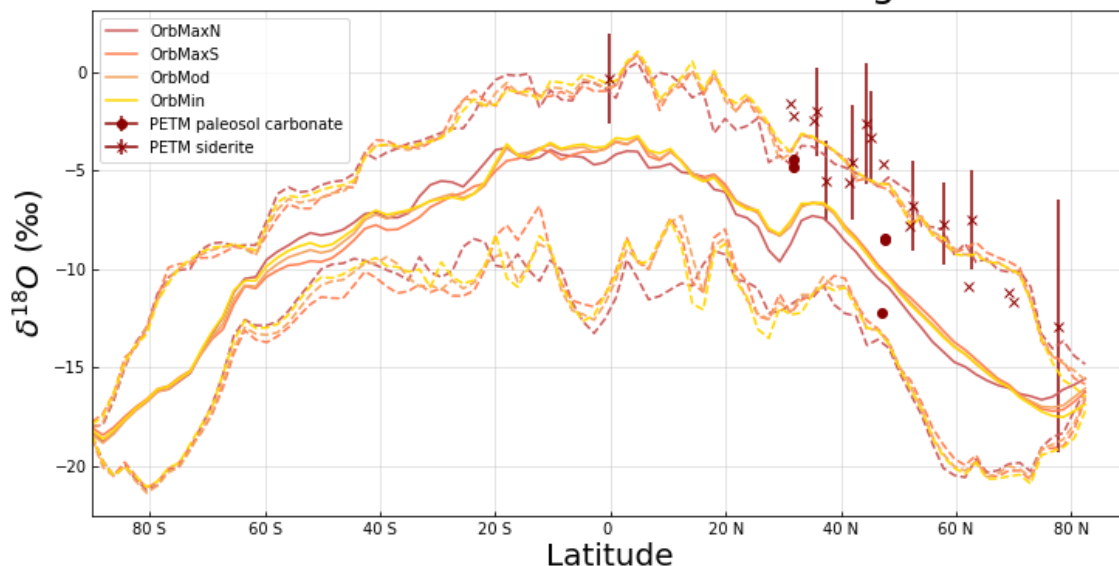


highest and lowest mean monthly soil water $\delta^{18}\text{O}$ or δD for all terrestrial longitudes at the given latitude for each orbital simulation, along with the mean annual values.

300 About 60% of PETM soil carbonate records fall within the simulated seasonal range for soil water $\delta^{18}\text{O}$, and several siderite
records fall above the highest monthly means, which likely represent the warm season (Fig. 9). In order to capture as many
proxy records as possible and not assume a particular seasonal time of formation, Fig. 9 displays the largest possible range
by utilizing the lowest and highest monthly modeled soil water $\delta^{18}\text{O}$ at each latitude. However, we also created the same
figure using specifically summer and winter means, though the range becomes tighter (Fig. A9). The siderite record may be
warm season biased, and the model may exhibit a slightly low $\delta^{18}\text{O}$ bias. Further assessment of model and proxy biases
305 contributing to this occurrence can be found in Sect. 4.

About 70% of PETM leaf wax records fall within the simulated seasonal range for model-inferred leaf wax δD (Fig. 10). In
order to capture as many proxy records as possible and not assume a particular seasonal time of formation, Fig. 10 displays
the largest possible range by utilizing the lowest and highest monthly model-inferred leaf wax δD at each latitude. However,
310 we also created the same figure using specifically summer and winter means, though the range becomes tighter (Fig. A10).
Records outside of the largest range may be seasonally biased or have a different fractionation factor than the model-inferred
values. Further assessment of model and proxy biases contributing to this occurrence can be found in Sect. 4.

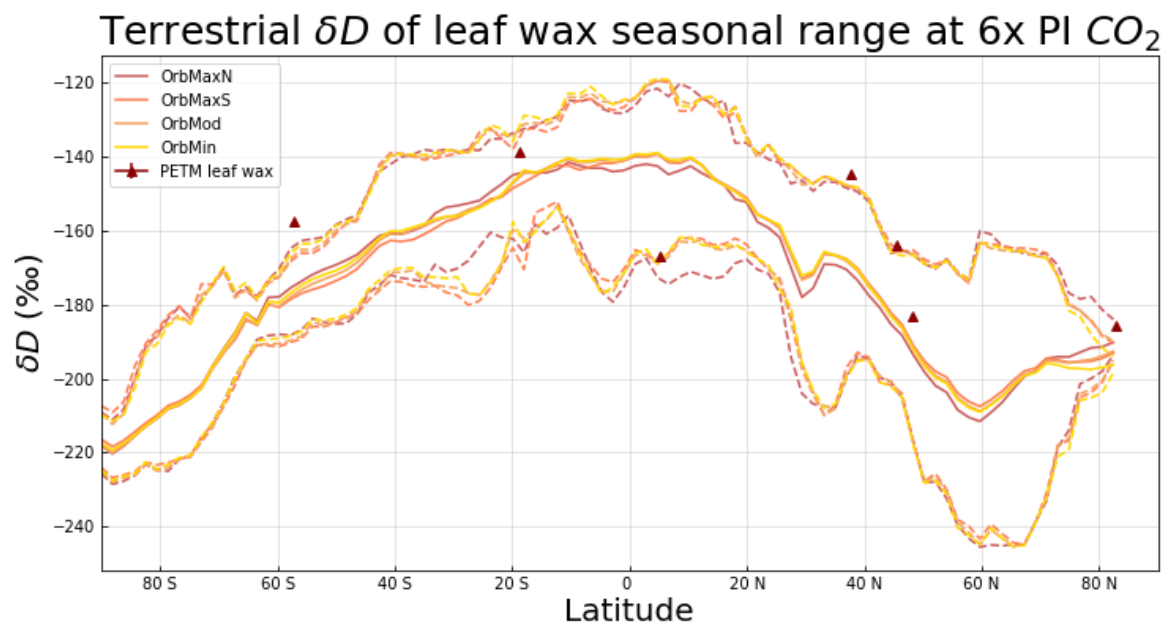
Terrestrial $\delta^{18}\text{O}$ of soil water seasonal range at 6x PI CO_2



315 **Figure 9: The simulated seasonal range of soil water $\delta^{18}\text{O}$ at a depth of 40-100 cm for each orbit under 6x PI CO_2 conditions compared to PETM paleosol carbonate and siderite $\delta^{18}\text{O}$ records. The middle line represents the mean annual soil water $\delta^{18}\text{O}$ at each latitude for all terrestrial longitudes, and the lower and upper dotted lines represent the lowest and highest monthly means at**



each latitude, respectively. The error bars represent uncertainty. The specific summer and winter means can be found in Figure A9.



320

Figure 10: The seasonal range of model-inferred leaf wax δD for each orbit under 6x PI CO_2 conditions compared to PETM leaf wax δD records. The middle line represents the mean annual leaf wax δD at each latitude for all terrestrial longitudes, and the lower and upper dotted lines represent the lowest and highest monthly means at each latitude, respectively. The specific summer and winter means can be found in Fig. A10.

325

The PETM was a relatively short period of extreme warming, and the eccentricity configuration would have remained almost constant during the onset. Furthermore, orbit has a substantial influence on climate, so a best guess as to the orbit during the onset of the PETM would impact our understanding of the PETM global warming and how it compares to present-day global warming. Figures 9 and 10 fail to emphasize orbital differences, as they only display zonal seasonal range, so this study

330

employs a quantitative point-by-point comparison method to emphasize orbital differences. The simulated 6x PI CO_2 $\delta^{18}O_p$ values are compared to the Van Dijk et al (2020) siderite PETM record to evaluate which orbital simulation is the best match. This record includes the widest span of latitudes and longitudes and analyzed several samples at each location to find a mean $\delta^{18}O$ value. In order to practically compare these proxy values to the simulated values, we found which group of 4

335

model grid cells captured the paleo-coordinates of each proxy location, and then found the mean of NH summer $\delta^{18}O$ values for that group of cells for each simulation. The siderite proxy values originate from the NH and appear to represent summer values (Table A1). The modeled summer days have been adjusted for the paleo-calendar effect (Bartlein and Shafer, 2019). Additionally, the global model grid cells may not represent the micro-climatic changes of the relevant regions, but the siderite records integrated data over hundreds to thousands of years, so the micro-climates of the recorded regions should not have a substantial impact on the measured isotopic ratio. The simulated $\delta^{18}O$ summer means at each of the ten locations were

340

then used to calculate the root mean square deviation (RMSD) calculated following Eq. (1):



$$RMSD = \sqrt{\frac{\sum_{i=1}^N (x_i - \hat{x}_i)^2}{N}}. \quad (1)$$

RMSD is commonly used for model-data comparisons (Flato et al., 2013; Thompson et al., 2022). The lower the result, the more comparable the simulated values are to the proxy values. The 6x PI CO₂ and OrbMaxN run is in best alignment with the proxy record. However, we are limited by the lack of SH Van Dijk records representing the PETM. The Van Dijk RMSD values are in bold (Table 3). We also decided to complete the RMSD with the other δ¹⁸O records (first number in parentheses), as well as the δD records (second number in parentheses), to see if their pattern of comparability would be consistent with the Van Dijk siderite record. All proxy records are more comparable to the 6x PI CO₂ simulations than the 3x PI CO₂ simulations since they are all from the PETM, but the orbital preferences varied (Table 3). Other hesitations, drawbacks, and speculations can be found in Sect. 4.

Root Mean Square Deviation	3x PI CO ₂	6x PI CO ₂
OrbMaxN	3.010 (3.426, 15.804)	2.652 (2.924, 14.263)
OrbMaxS	4.932 (3.354, 14.457)	3.323 (2.262, 13.924)
OrbMin	4.338 (3.196, 15.667)	3.059 (2.436, 14.436)
OrbMod	4.260 (3.298, 15.517)	3.149 (2.437, 14.288)

Table 3: The calculated RMSD for each simulated case compared to the Van Dijk siderite record (in bold). The parentheses hold the calculated RMSD for each simulated case compared to the other δ¹⁸O records, as well as the δD records, respectively.

4 Discussion

No climate model perfectly reproduces Earth's past, but they can provide a window to large-scale patterns and be verified through model-data comparisons, as well as paint the environmental context for proxy records. Our model simulated four orbits at two different atmospheric CO₂ settings and traced water isotopic ratios to allow for comparisons to various water isotope proxy records. A past study using a lower resolution model of the Early Eocene found a heavy influence of orbit on seasonal precipitation trends during the Early Eocene and our findings agree (Keery et al., 2018). OrbMaxS and OrbMaxN simulations exhibit high eccentricity and obliquity, resulting in intense seasonality, but different orbital precession, resulting in dramatic differences in insolation distribution seasonally (Fig. A3). These two orbital experiments also show a narrowed width of the ITCZ, as well as ITCZ migration towards the hemisphere with maximum summer insolation, which may provide more moisture to the SH (NH) in OrbMaxS (OrbMaxN) (Figs. 3, 6, A8, Burns et al., 2022). For instance, our findings agree with a past study that found enhanced precipitation in southeastern Asia during June for OrbMaxN (Fig. 3, Kiehl et al., 2018).



370 We find dramatic differences in $\delta^{18}\text{O}_p$ between OrbMaxS and OrbMaxN as a result of seasonal changes in insolation,
reaching up to $\sim 6.5\%$ in certain regions (Fig. 4). The differences in $\delta^{18}\text{O}_p$ between the two CO_2 background states were less
dramatic, reaching only $\sim 3.0\%$ in certain regions (Fig. 7). Key regions of interest (those experiencing the greatest
differences in oxygen isotopic signals) show greater changes in $\delta^{18}\text{O}_p$ in response to orbital change than a CO_2 doubling due
to higher seasonal sensitivity. However, the simulations with doubled CO_2 showed a consistent, mean annual increase in
375 $\delta^{18}\text{O}_p$, which orbital changes are less likely to provoke. Therefore, changes in precession play an important role on the
hydrologic cycle seasonally and is a valuable piece of information to consider when interpreting paleo-records – especially
when those records form over shorter periods of time and are seasonally biased.

Some paleosol carbonate proxies most closely match maximum simulated soil water $\delta^{18}\text{O}$, which represent summer values,
380 though not all (Fig. 9). This comparison is consistent with the idea that paleosol carbonates sometimes preserve a signal of
the isotopic composition of rainfall during the warmer, more evaporative season in which the carbonates may be more likely
to form (Kelson et al., 2020). The siderite records appear to fall along the maximum $\delta^{18}\text{O}$ simulated values for all modeled
cases, signaling a possible warm-season bias. Recent studies argue that pedogenic siderite forms between the mean annual
air temperature and the mean air temperature of the warmest months, depending on the latitude (Fernandez et al., 2014; van
385 Dijk et al., 2019). Some temperature reconstructions support that siderite forms more rapidly under warmer, more evaporitic
conditions, especially in higher latitudes, since it's controlled by microbial iron reduction which proceeds faster in higher
soil temperatures (van Dijk et al., 2020). Therefore, both archives likely have some records that represent the soil water $\delta^{18}\text{O}$
during the warm, dry, evaporative season when they are more likely to form, but especially the siderite. As siderite appeared
consistently warm season biased, we chose to use the summertime average soil temperature for the siderite PSM.

390 The terrestrial $\delta^{18}\text{O}$ proxy records span much of the NH, but are lacking in the SH, limiting our model-data comparison.
Although the model's paleo-elevation roughly matches the paleo-elevation estimates from the proxy records, proxies from
the highest elevations were excluded because paleo-altimetry estimates have larger uncertainty. Aside from the seasonal
bias, the exclusion of high elevation proxies may explain why none of the records sit closer to the minimum $\delta^{18}\text{O}$ values, as
395 areas of high elevation often result in low $\delta^{18}\text{O}$, though this is not necessarily the case under high CO_2 conditions
(Dansgaard, 1964). Additionally, there is evidence that iCESM1.2 has a slight low bias for $\delta^{18}\text{O}_p$, which may transfer to the
 $\delta^{18}\text{O}$ of soil water and drive further misalignment between model and proxies (Brady et al., 2019). Other limitations in this
model-data comparison may include the possibility of evaporation before burial, diagenesis, uncertainty in timing, varying
elevations, or error in paleo-coordinate conversion or fractionation factor.

400



Furthermore, the terrestrial δD proxy records largely fall within the simulated seasonal range for model-inferred leaf wax δD (Fig. 10). One record is closer to the minimum δD , likely because that record was taken from a tropical rainforest with increased and D-depleted rainfall, but the other records align closer to mean or maximum δD (Fig. 10, Jaramillo et al., 2010). Leaves undergo transpiration while growing, an evaporative process that further fractionates water isotopes, which
405 often result in D-enrichment of leaf water and has a critical effect on the final δD of leaf wax n-alkanes (Kahmen et al., 2013). Therefore, it is likely that some records align closer to maximum δD values in part due to transpiration. Leaves also tend to grow over a matter of weeks, so seasonal bias and short-term formation could be another reason for slight mismatches between the model and data. Plus, the fractionation factor used in the WaxPSM is a globally averaged estimate, so that could account for some mismatch. Aside from that, some of the same limitations faced in the $\delta^{18}O$ comparison are
410 also relevant in the δD comparison – uncertainty in timing, varying elevations, or error in paleo-coordinate conversion. However, the majority of leaf wax records fall within the model-inferred seasonal range of leaf wax δD .

Finally, previous studies indicated that Earth experienced near-maximum solar irradiance at the onset of the PETM largely due to variations in eccentricity (Zeebe et al., 2017; Lourens et al., 2005; Westerhold et al., 2009; Zachos et al., 2010;
415 Galeotti et al., 2010; Westerhold et al., 2012). Several studies argue that the Earth's eccentricity at this time may have partly caused the extreme warming during the PETM, and our findings agree (Kiehl et al., 2018; Lawrence et al., 2003). The Kiehl et al (2018) study also argues that the Earth was likely experiencing an orbit most similar to OrbMaxN at the onset of the PETM (Table 3). Although it is worth constraining the orbit at the onset of the PETM in order to further understand the relatively rapid and extreme warming that followed, there are several limitations to this model-data comparison that render it
420 less effective. There are biases with the oxygen isotope records, discussed above, and several drawbacks of the simulations, including the resolution and model bias. These model simulations are run with a relatively coarse atmosphere (~2-degree horizontal resolution) and topography, which may not fully capture the local environments of the proxy records. Perhaps most importantly, the timing of the onset of the PETM is not perfectly constrained so the proxy records may not represent the onset itself. So aside from the van Dijk siderite record, we also conducted an RMSD for the other PETM proxy records to
425 speculate on what consistent (or inconsistent) patterns between simulations could mean. All records match the higher CO_2 level better than the lower CO_2 level within the same orbit, which was expected with PETM records (Table 3). However, the other $\delta^{18}O$ records did not match OrbMaxN best, but rather matched OrbMaxS best at the PETM greenhouse gas level. The δD records seem to favor OrbMaxS as well, if anything. Given the variability within the RMSD, we hesitate to draw any strong conclusions, but we speculate that the records all likely formed during varying orbits or were slightly more likely to
430 form during orbital times of maximum seasonality.

Determining the potential orbit in existence at this time can contribute to our knowledge of how this past global warming differs from our present-day global warming. For instance, the 6x PI CO_2 and OrbMaxN modeled run is relatively far from our present-day warming scenario. The current atmospheric CO_2 concentration is about $\frac{1}{4}$ as high, and the 6x PI CO_2



435 OrbMaxN simulation has a mean annual global temperature 0.71°C higher than the 6x PI CO_2 OrbMod simulation, largely
driven by the higher insolation maximum of OrbMaxN. If the 6x PI CO_2 OrbMaxN simulation is the closest to representing
the onset of the PETM, this highlights how the PETM differs from modern climate in important ways that constrain its use as
an analogue for the Anthropocene, especially since a maximum NH summer insolation orbit would have slightly bolstered
global warming during the PETM, unlike our modern orbit.

440

5 Conclusions

This study demonstrates the relative impact of CO_2 and orbit on climate and the orbital sensitivity of the hydrologic cycle
under different CO_2 background states through the combination of a fully coupled climate model suite of the Early Eocene
and published terrestrial $\delta^{18}\text{O}$ and δD proxy records. Our results reveal that orbit can have a more substantial impact on the
hydrologic cycling than doubling CO_2 in certain regions seasonally, although doubling CO_2 has a more consistent and
global-scale impact, and that orbital sensitivity weakens under a higher CO_2 background state. The comparison to terrestrial
 $\delta^{18}\text{O}$ and δD records verifies the reliability of our model and lends some interpretation to the biases within iCESM and the
environmental context pertaining to the potential warm-season bias of some of the proxies so we may better understand what
they represent. The iCESM generally performs well in simulating hydrologic cycling during a warmer climate, which
increases trust in iCESM to project future climate change. Exploring OrbMaxN as a potential cause for the onset of the
PETM is worthwhile, though many uncertainties in the model-data comparison exist. Simulating the Early Eocene is
valuable as it experienced high CO_2 levels, heightened seasonality, and precipitation extremes, which we expect with future
climate change. These simulations further our understanding of the role CO_2 and orbit play in climate change and the
hydrologic cycle.

455

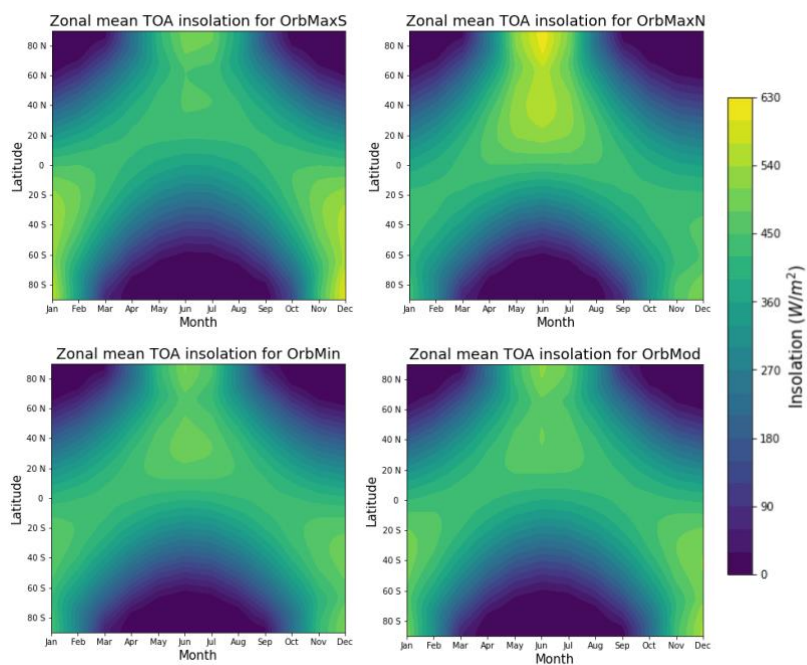
Appendix A

Modern Coordinates ($^{\circ}\text{N}$, $^{\circ}\text{E}$)	Paleo Coordinates ($^{\circ}\text{N}$, $^{\circ}\text{E}$)	Grid Cells (Lat, Lon)
62, -6.5	57.88, -10.4	78-79, 139-140
33.4, -117.2	37.36, -99.78	67-68, 104-105
75.3, 135.5	77.69, 128.26	88-89, 51-52
34.55, -92.51	35.8, -74.96	66-67, 114-115
47.32, -122	52.49, -102.24	75-76, 103-104
56.33, -133.22	62.66, -111.69	80-81, 99-100
4, -72	-0.24, -58.7	47-48, 120-121



39.02, -104.27	41.92, -85.8	69-70, 109-110
41.99, -106.44	45.15, -87.26	71-72, 109-110
49, 2.2	44.3, -0.95	70-71, 142-143

460 **Table A1:** The modern and paleo-coordinates for each van Dijk (2020) proxy location, followed by the appropriate model grid cells.



465 **Figure A1:** The zonal, monthly top-of-atmosphere (TOA) solar insolation distribution for all orbits. OrbMaxS and OrbMaxN reach a higher summer insolation than OrbMod or OrbMin.

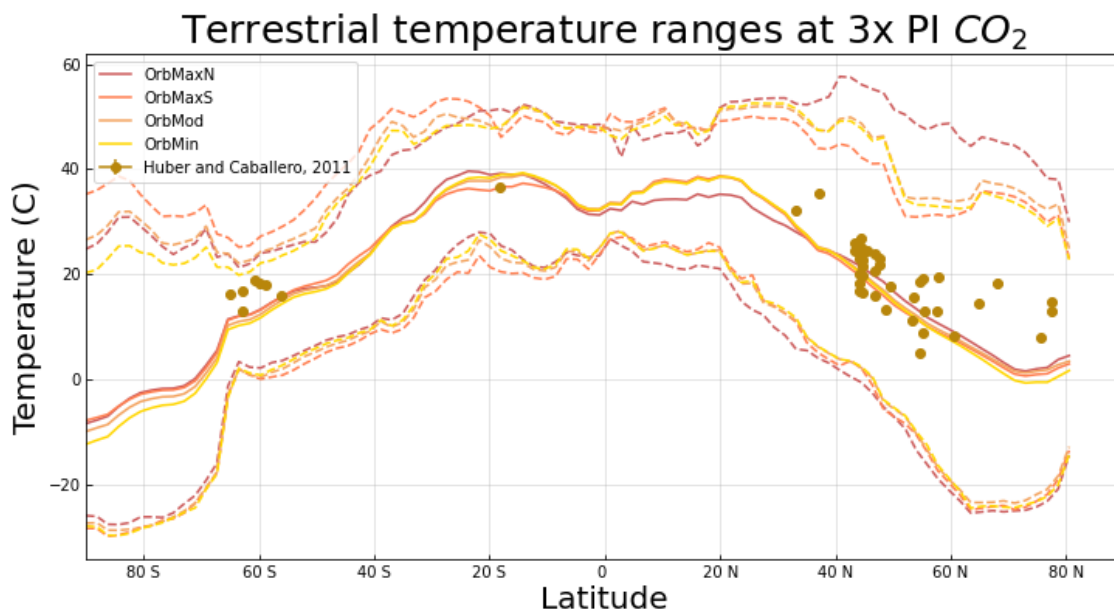


Figure A2: Model-data comparison between the Huber & Caballero (2011) Eocene terrestrial dataset and the 3X PI CO₂ simulations. The middle solid line represents the mean annual at each latitude for all terrestrial longitudes, and the lower and upper dotted lines represent the lowest and highest monthly means at each latitude, respectively.

470

Seasonal TOA insolation differences (OrbMaxS - OrbMaxN)

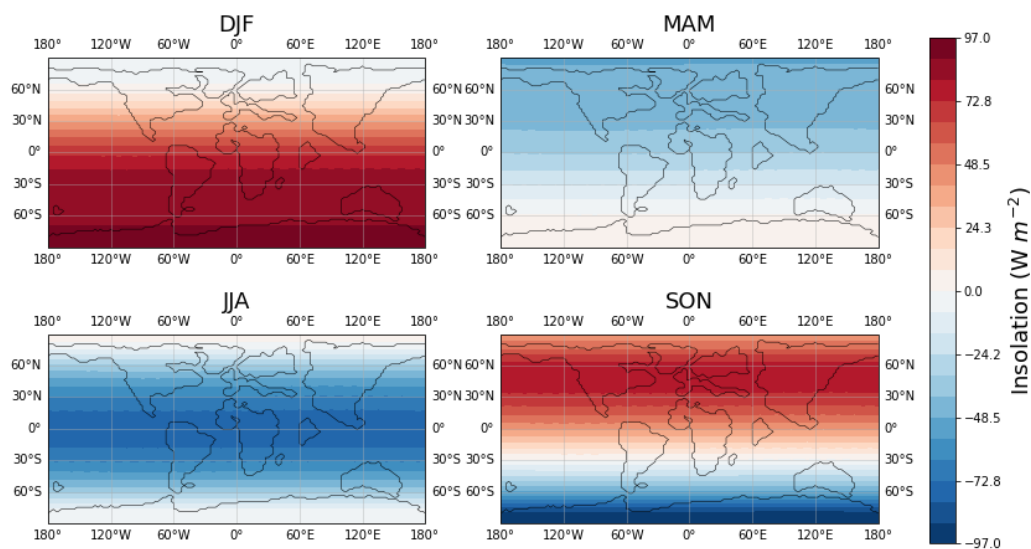
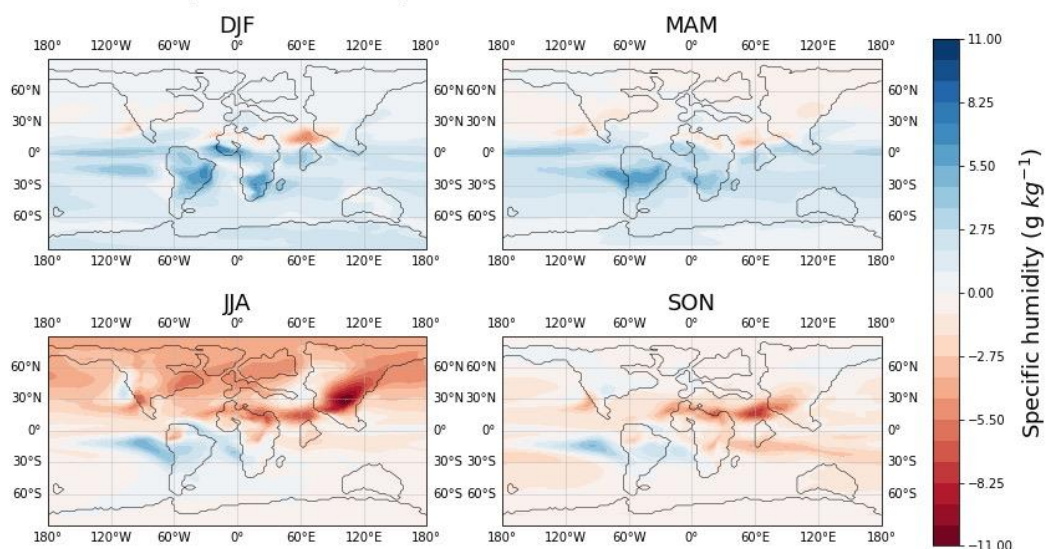


Figure A3: The seasonal zonal top-of-atmosphere (TOA) solar insolation difference between OrbMaxS and OrbMaxN.

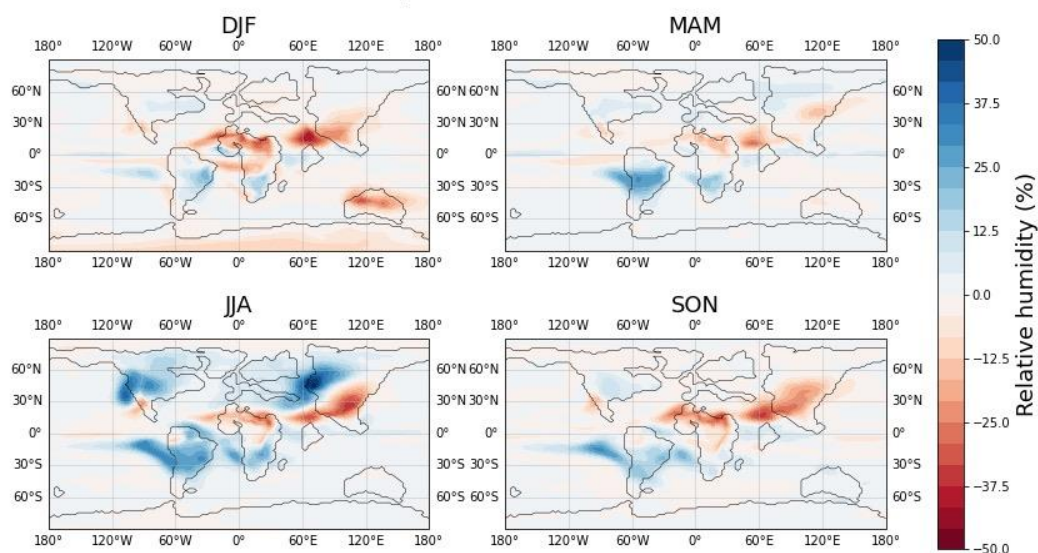


Seasonal specific humidity differences (OrbMaxS - OrbMaxN) at 3x PI CO₂



475 **Figure A4:** The seasonal specific humidity differences between OrbMaxS and OrbMaxN at 3x PI CO₂. Specific humidity is presented here at 850 atmosphere hybrid sigma pressure coordinates. Sigma coordinates represent pressure at the Earth's surface rather than the mean sea level, so it follows the actual terrain. We chose these coordinates because they represent the same pressure level above the land without running into mountains.

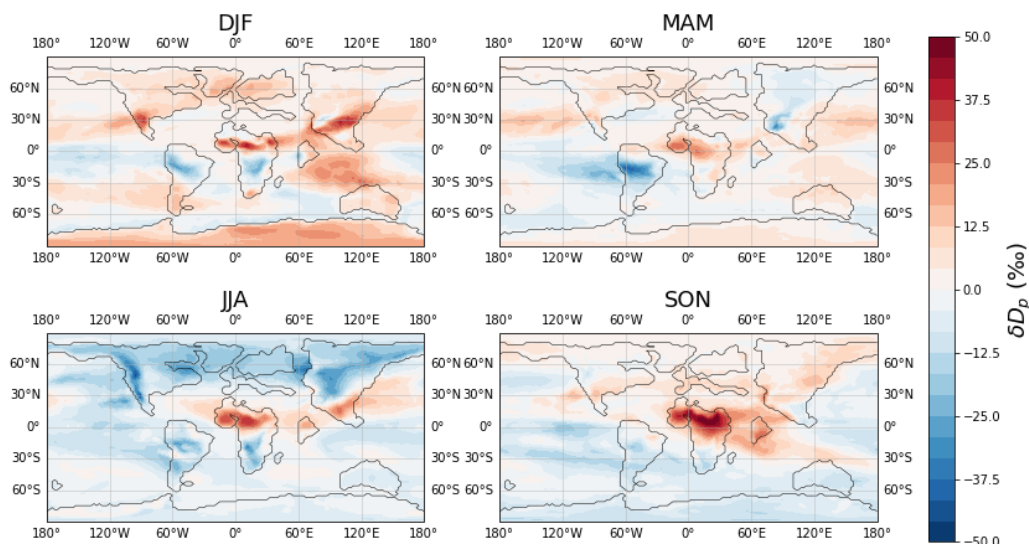
Seasonal relative humidity differences (OrbMaxS - OrbMaxN) at 3x PI CO₂



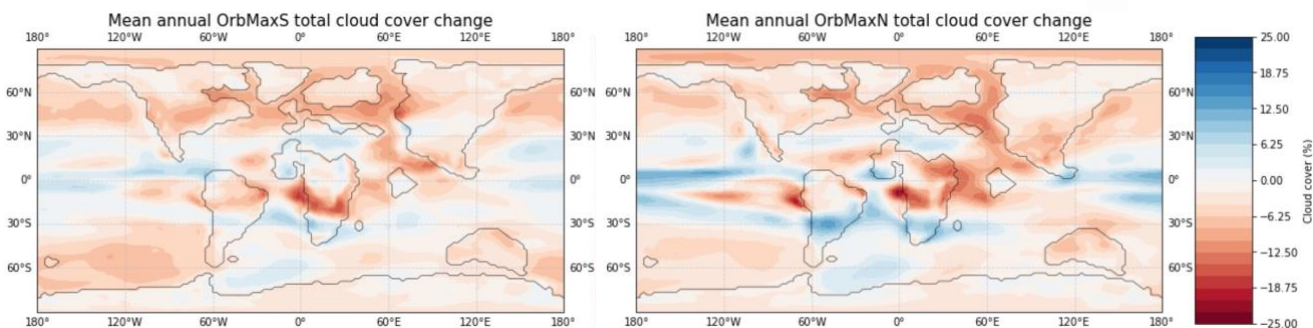
480 **Figure A5:** The seasonal relative humidity differences between OrbMaxS and OrbMaxN at 3x PI CO₂. Relative humidity is presented here at 850 atmosphere hybrid sigma pressure coordinates. Sigma coordinates represent pressure at the Earth's surface rather than the mean sea level, so it follows the actual terrain. We chose these coordinates because they represent the same pressure level above the land without running into mountains.



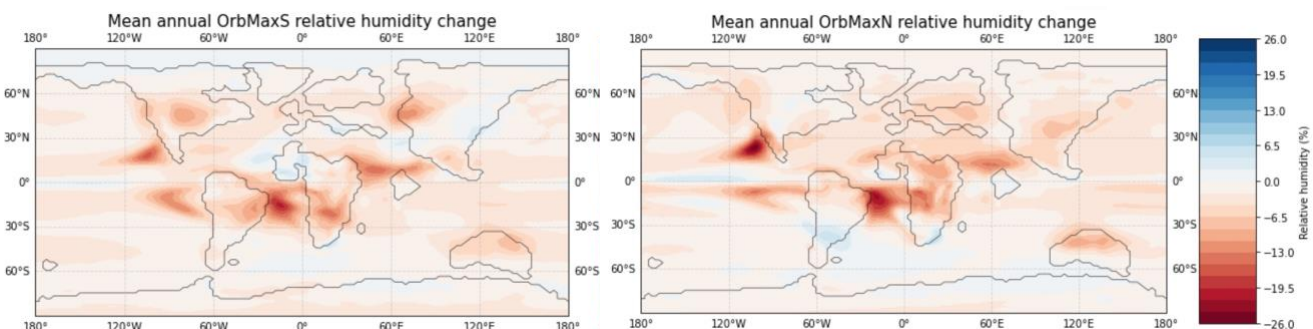
Seasonal δD_p differences (OrbMaxS - OrbMaxN) at 3x PI CO₂



485 **Figure A6: The seasonal δD_p differences between OrbMaxS and OrbMaxN at 3x PI CO₂.**



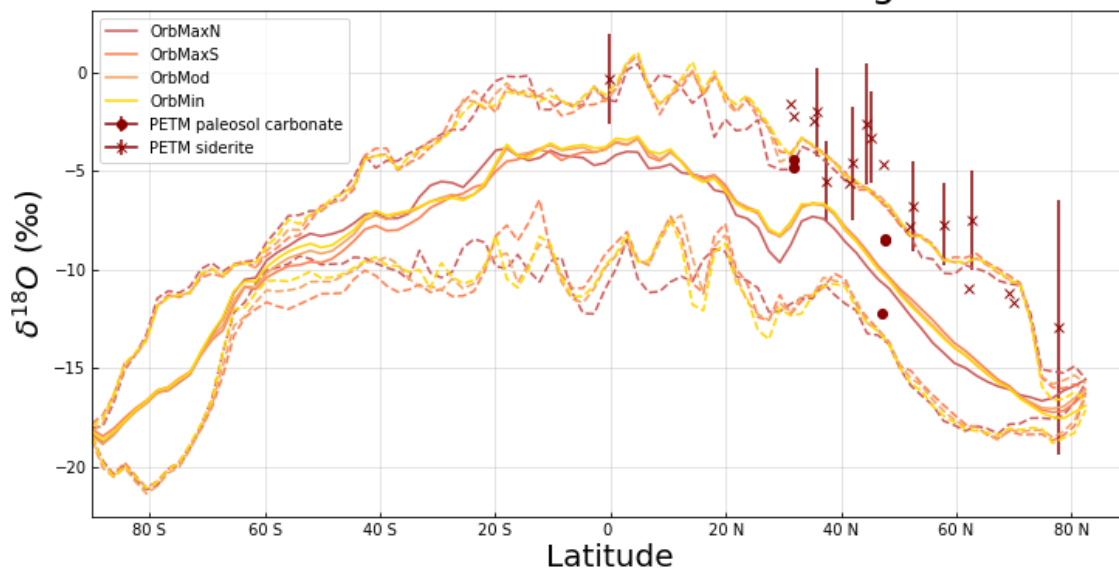
490 **Figure A7: The difference in mean annual total cloud coverage under 6x PI CO₂ compared to 3x PI CO₂ for OrbMaxS (left) and OrbMaxN (right).**



495 **Figure A8: The difference in mean annual relative humidity at 6x PI CO₂ compared to 3x PI CO₂ for OrbMaxS (left) and OrbMaxN (right). Relative humidity is presented here at 850 atmosphere hybrid sigma pressure coordinates. Sigma coordinates represent pressure at the Earth's surface rather than the mean sea level, so it follows the actual terrain. We chose these coordinates because they represent the same pressure level above the land without running into mountains.**

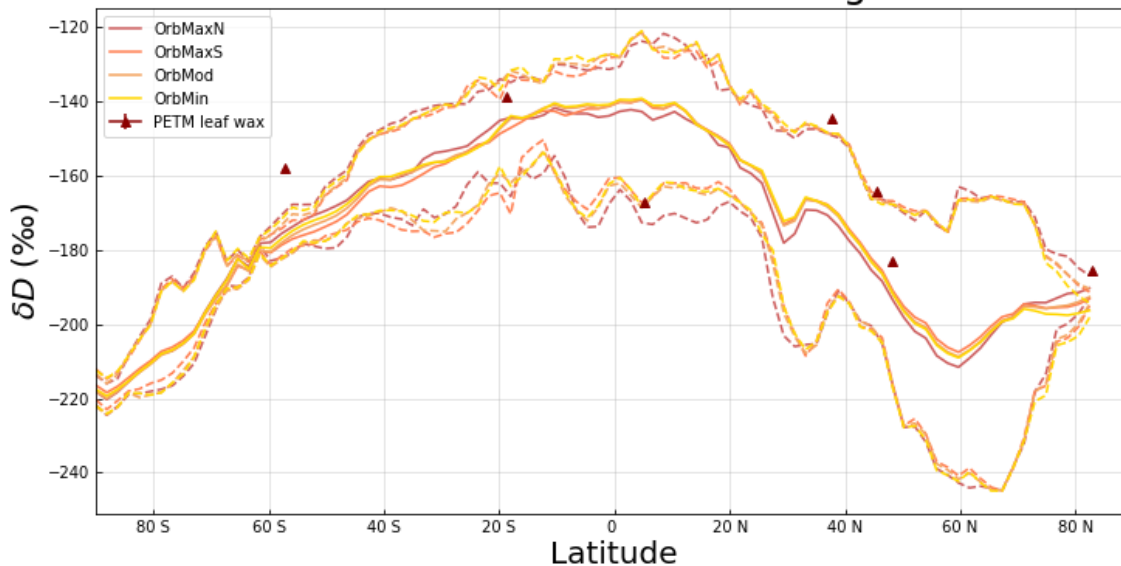


Terrestrial $\delta^{18}\text{O}$ of soil water seasonal range at 6x PI CO_2

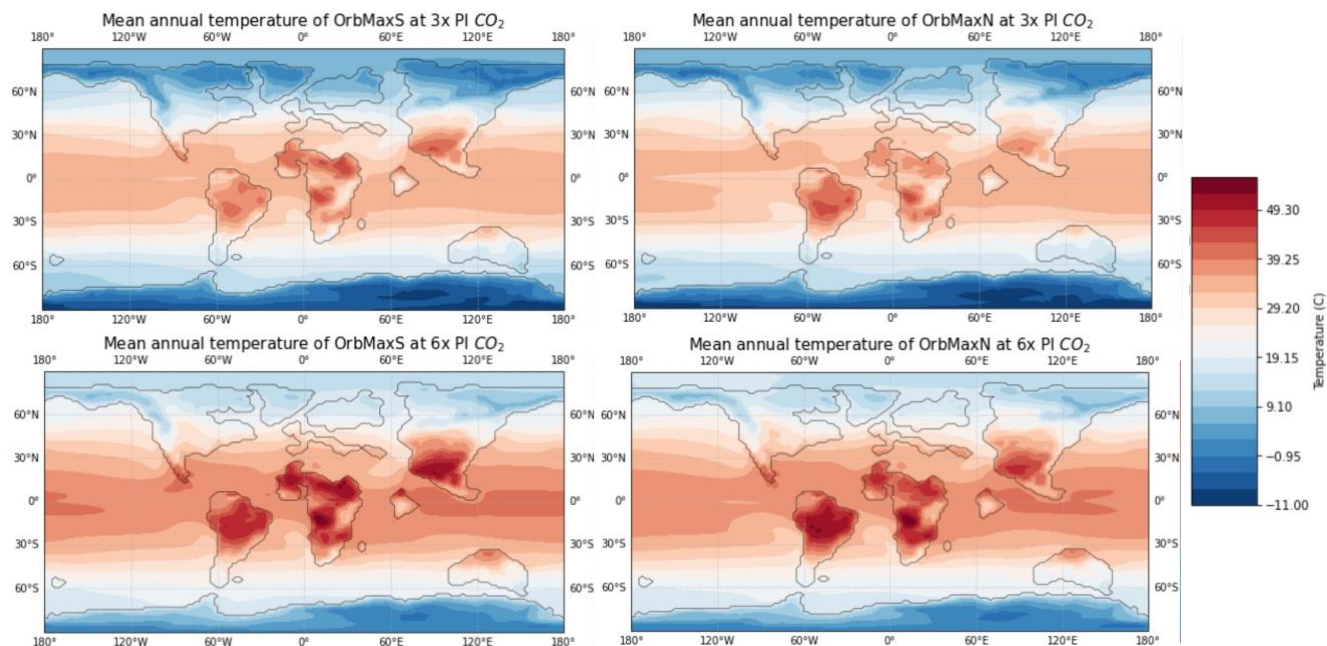


500 **Figure A9:** The simulated seasonal range of soil water $\delta^{18}\text{O}$ at a depth of 40-100 cm for each orbit under 6x PI CO_2 conditions compared to PETM paleosol carbonate and siderite $\delta^{18}\text{O}$ records. The middle line represents the mean annual soil water $\delta^{18}\text{O}$ at each latitude for all terrestrial longitudes, and the lower and upper dotted lines represent the winter and summer means at each latitude, respectively. The error bars represent uncertainty.

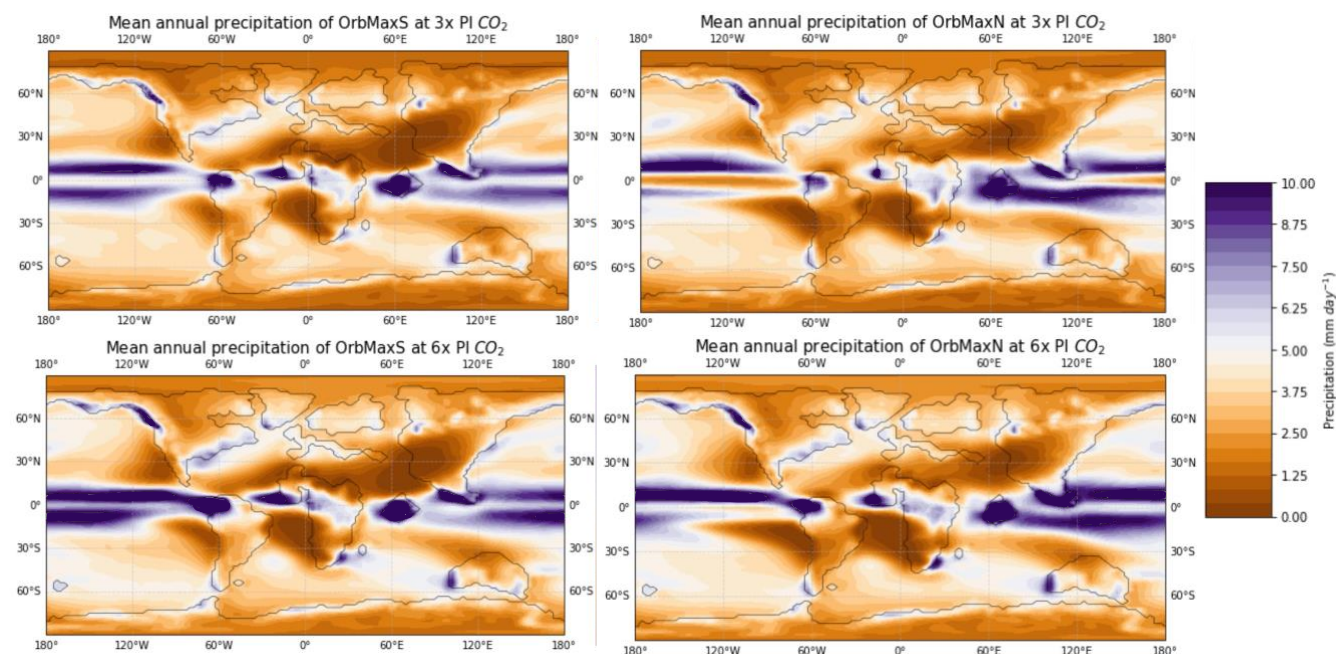
Terrestrial δD of leaf wax seasonal range at 6x PI CO_2



505 **Figure A10:** The seasonal range of model-inferred leaf wax δD for each orbit under 6x PI CO_2 conditions compared to PETM leaf wax δD records. The middle line represents the mean annual leaf wax δD at each latitude for all terrestrial longitudes, and the lower and upper dotted lines represent the winter and summer means at each latitude, respectively.



510 **Figure A11:** The mean annual surface air temperature at 3x PI CO₂ (above) and 6x PI CO₂ (below) for OrbMaxS (left) and OrbMaxN (right).



515 **Figure A12:** The mean annual precipitation at 3x PI CO₂ (above) and 6x PI CO₂ (below) for OrbMaxS (left) and OrbMaxN (right). The maximum positive precipitation difference on the corresponding color bar represents anything experiencing 10.00 mm day⁻¹ or higher.

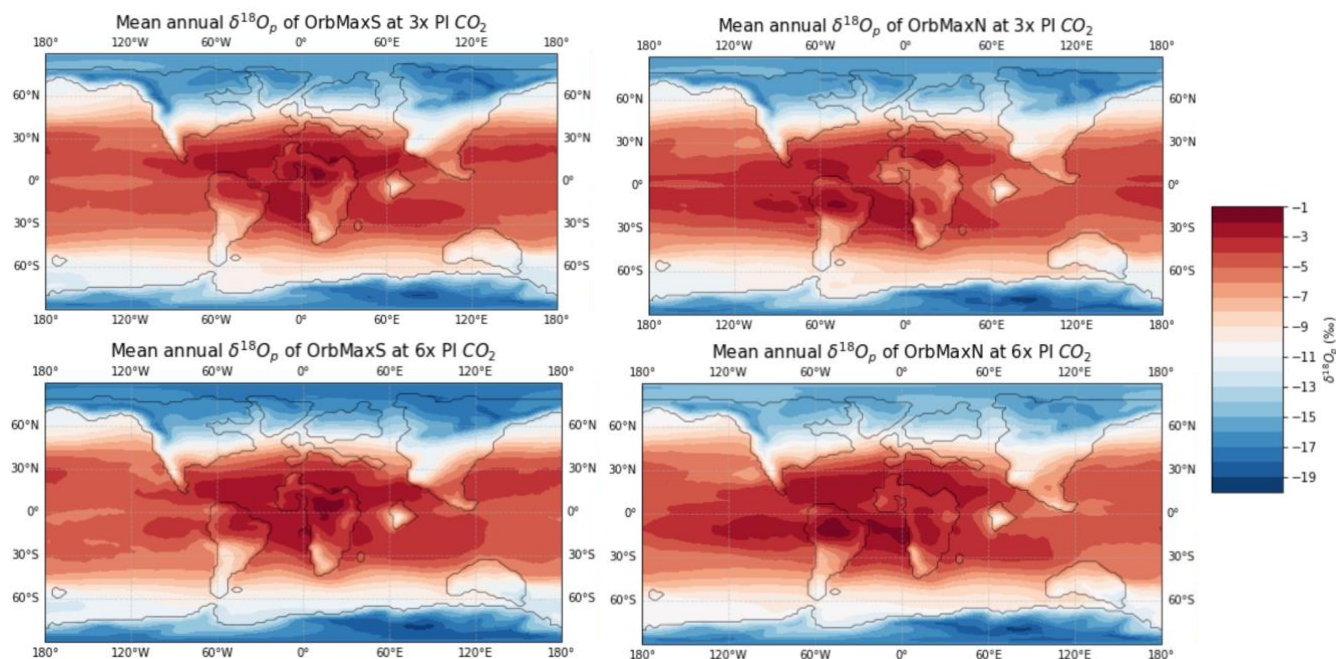


Figure A13: The mean annual $\delta^{18}\text{O}_p$ at 3x PI CO_2 (above) and 6x PI CO_2 (below) for OrbMaxS (left) and OrbMaxN (right).

520

Code and data availability

All data needed to evaluate the conclusions in the paper are presented in the paper. The published proxy records used in this study are all cited. Additional data related to this paper are available in the Zenodo repository (doi: 10.5281/zenodo.7971738). Additional data are provided on request to the authors. The CESM model code is available through the National Center for Atmospheric Research software development repository (525 https://svn-ccsm-models.cgd.ucar.edu/cesm1/exp_tags/pcesm_cesm1_2_2_tags/dt-cesm1.0_cesm1_2_2_1/).

Author contributions

JC and CP designed the experimental approach. JC analyzed the results and prepared the figures. JZ developed the model code and performed the simulations. JT provided proxy data. JK provided code templates for analysis. JC prepared the manuscript and all co-authors provided comments. (530

Competing interests

The authors declare that they have no conflict of interest.

535

Acknowledgements

This research has been supported by the National Science Foundation (grant no. 2002397).



References

- 540 Bartlein, P. and Shafer, S.: Paleo calendar-effect adjustments in time-slice and transient climate-model simulations: Impact and strategies for data analysis, *Geosci. Model Dev.*, 12, 3889-3913, <https://doi.org/10.5194/gmd-12-3889-2019>, 2019.
- Bataille, C., Watford, D., Ruegg, S., Lowe, A., and Bowen, G.: Chemostratigraphic age model for the Tornillo Group: A possible link between fluvial stratigraphy and climate, *Palaeogeogr. Palaeoclimatol.*, 457, 277-289, <https://doi.org/10.1016/j.palaeo.2016.06.02>, 2016.
- 545 Berger, A.: Milankovitch theory and climate, *Rev. Geophys.*, 26, 624-657, <https://doi.org/10.1029/RG026i004p00624>, 1988.
- Bowen, G., Maibauer, B., Kraus, M., Rohl, U., Westerhold, T., Steimke, A., Gingerich, P., Wing, S., and Clyde, W.: Two massive, rapid releases of carbon during the onset of the Paleocene-Eocene thermal maximum, *Nat. Geosci.*, 8, 44-47, <https://doi.org/10.1038/ngeo2316>, 2014.
- 550 Brady, E., Stevenson, S., Bailey, D., Liu, Z., Noone, D., Nusbaumer, J., Otto-Bliesner, B., Tabor, C., Tomas, R., Wong, T., Zhang, J., and Zhu, J.: The connected isotopic water cycle in the community earth system model version 1, *J. Adv. Model Earth Syst.*, 11, 2547-2566, <https://doi.org/10.1029/2019MS001663>, 2019.
- 555 Burgener, L., Huntington, K., Hoke, G., Schauer, A., Ringham, M., Latorre, C., and Diaz, F.: Variations in soil carbonate formation and seasonal bias over >4 km of relief in the western Andes revealed by clumped isotope thermometry, *Earth Planet Sc. Lett.*, 441, 188-199, <https://doi.org/10.1016/j.epsl.2016.02.03>, 2016.
- 560 Burns, S., McGee, D., Scroxton, N., Kinsley, C., Godfrey, L., Faina, P., and Ranivoharimanana, J.: Southern hemisphere controls on ITCZ variability in southwest Madagascar over the past 117,000 years, *Quaternary Science Reviews*, 276, <https://doi.org/10.1016/j.quascirev.2021.107317>, 2022.
- 565 Byrne, M. and O’Gorman, P.: Land-ocean warming contrast over a wide range of climates: Convective quasi-equilibrium theory and idealized simulations, *J. Climate*, 26, 4000-4016, <https://doi.org/10.1175/jcli-d-12-00262.1>, 2013.
- Craig, H.: Isotopic variations in meteoric waters, *Science*, 133, 1702-1703, <https://doi.org/10.1126/science.133.3465.1702>, 1961.



- 570 Dansgaard, W.: Stable isotopes in precipitation, *Tellus*, 16, 436-468, <https://doi.org/10.1111/j.2153-3490.1964.tb00181.x>, 1964.
- Davis, B. and Brewer, S.: A unified approach to orbital, solar, and lunar forcing based on the earth's latitudinal insolation/temperature gradient, *Quaternary Science Reviews*, 30, 1861-1874,
575 <https://doi.org/10.1016/j.quascirev.2011.04.016>, 2011.
- Dong, B., Gregory, J., and Sutton, R.: Understanding land-sea warming contrast in response to increasing greenhouse gases, Part I: Transient adjustment, *J. Climate*, 22, 3079-3097, <https://doi.org/10.1175/2009JCLI2652.1>, 2009.
- 580 Douville, H., Raghavan, K., and Renwick, J.: Water cycle changes, in: *Climate Change 2021: The Physical Science Basis. Contribution of working group I to the sixth assessment report of the Intergovernmental Panel on Climate Change.* Cambridge University Press, 1055-1210, <https://doi.org/10.1017/9781009157896.010>, 2021.
- Fernandez, A., Tang, J., and Rosenheim, B.: Siderite 'clumped' isotope thermometry: A new paleoclimate proxy for humid
585 continental environments, *Geochim. Cosmochim. Ac.*, 126, 411-421, <https://doi.org/10.1016/j.gca.2013.11.006>, 2014.
- Flato, G. and Marotzke, J.: Evaluation of climate models, in: *Climate Change 2013: The Physical Science Basis. Contribution of working group I to the fifth assessment report of the Intergovernmental Panel on Climate Change.* Cambridge University Press, 741-866, <https://doi.org/10.1017/CBO9781107415324>, 2013.
- 590 Friedman, I. and O'Neil, J.: Compilation of stable isotope fractionation factors of geochemical interest, in: *Data of Geochemistry*, USGS, <https://doi.org/10.3133/pp440KK>, 1977.
- Galeotti, S., Krishnan, S., Pagani, M., Lanci, L., Gaudio, A., Zachos, J., Monechi, S., Morelli, G., and Lourens, L.: Orbital
595 chronology of early Eocene hyperthermals from the Contessa Road section, central Italy, *Earth Planet Sc. Lett.*, 290, 192-200, 192-200. <https://doi.org/10.1016/j.epsl.2009.12.021>, 2010.
- Garel, S., Schnyder, J., Jacob, J., Dupuis, C., Boussafir, M., Milbeau, C., Storme, J-Y., Iakovleva, A., Yans, J., Baudin, F., Flehoc, C., and Quesnel, F.: Paleohydrological and paleoenvironmental changes recorded in terrestrial sediments of the
600 Paleocene-Eocene boundary (Normandy, France), *Palaeogeogr. Palaeoclimatol.*, 376, 184-199, <https://doi.org/10.1016/j.palaeo.2013.02.035>, 2013.



- 605 Handley, L., Crouch, E., and Pancost, R.: A New Zealand record of sea level rise and environmental change during the Paleocene-Eocene thermal maximum, *Palaeogeogr. Palaeoclimatol., 305*, 185-200, <https://doi.org/10.1016/j.palaeo.2011.03.001>, 2011.
- 610 Handley, L., Pearson, P., McMillan, I., and Pancost, R.: Large terrestrial and marine carbon and hydrogen isotope excursions in a new Paleocene/Eocene boundary section from Tanzania, *Earth Planet. Sc. Lett.*, *275*, 17-25, <https://doi.org/10.1016/j.epsl.2008.07.030>, 2008.
- Herold, N., Buzan, J., Seton, M., Goldner, A., Green, J. A. M., Müller, R. D., Markwick, P., and Huber, M.: A suite of early Eocene (~ 55 Ma) climate model boundary conditions, *Geosci. Model Dev.*, *7*, 2077–2090, <https://doi.org/10.5194/gmd-7-2077-2014>, 2014.
- 615 Huber, M. and Caballero, R.: The early Eocene equable climate problem revisited, *Clim. Past*, *7*, 603-633, <https://doi.org/10.5194/cp-7-603-2011>, 2011.
- Hurrell, J., Holland, M., Gent, P., Ghan, S., Kay, J., Kushner, P., Lamarque J., Large, W., Lawrence, D., Lindsay, K., Lipscomb, W., Long, M., Mahowald, N., Marsh, D., Neale, R., Rasch, R., Vavrus, S., Vertenstein, M., Bader, D., Collins, W., Hack, J., Kiehl, J., and Marshall, S.: The community earth system model: A framework for collaborative research, *Bull. Amer. Meteor. Soc.*, *94*, 1339-1360, <https://doi.org/10.1175/bams-d-12-00121.1>, 2013.
- 625 Jaramillo, C., Ochoa, D., Contreras, L., Pagani, M., Carvajal-Ortiz, H., Pratt, L., Krishnan, S., Cardonna, A., Romero, M., Quiroz, L., Rodriguez, G., Rueda, M., de la Parra, F., Moron, S., Green, W., Bayona, G., Montes, C., Quintero, O., Ramirez, R., Mora, G., Schouten, S., Bermudez, H., Navarrete, R., Parra, F., Alvaran, M., Osorno, J., Crowley, J., Valencia, V., and Vervoort, J.: Effects of rapid global warming at the Paleocene-Eocene boundary on neotropical vegetation, *Science*, *330*, 957-961, <https://doi.org/10.1126/science.1193833>, 2010.
- 630 Kahmen, A., Hoffmann, B., Schefub, E., Arndt, S., Cernusak, L., West, J., and Sachse, D.: Leaf water deuterium enrichment shapes leaf wax n-alkane δD values of angiosperm plants II: Observational evidence and global implications, *Geochim. Cosmochim. Ac.*, *111*, 50-63, <https://doi.org/10.1016/j.gca.2012.09.004>, 2013.
- Keery, J., Holden, P., and Edwards, N.: Sensitivity of the Eocene climate to CO₂ and orbital variability, *Clim. Past*, *14*, 215-238, <https://doi.org/10.5194/cp-14-215-2018>, 2018.

635



- Kelson, J., Huntington, K., Breecker, D., Burgener, L., Gallagher, T., Hoke, G., and Petersen, S.: A proxy for all seasons? A synthesis of clumped isotope data from Holocene soil carbonates, *Quaternary Science Reviews*, 234, <https://doi.org/10.1016/j.quascirev.2020.106259>, 2020.
- 640 Kelson, J., Watford, D., Bataille, C., Huntington, K., Hyland, E., and Bowen, G.: Warm terrestrial subtropics during the Paleocene and Eocene: Carbonate clumped isotope evidence from the Tornillo Basin, Texas (USA), *Paleoceanography and Paleoclimatology*, 33, 1230-1249, <https://doi.org/10.1029/2018pa003391>, 2018.
- Kiehl, J., Shields, C., Snyder, M., Zachos, J., and Rothstein, M.: Greenhouse and orbital forced climate extreme during the
645 early Eocene, *Philos. T. R. Soc. A*, 376, <https://doi.org/10.1098/rsta.2017.0085>, 2018.
- Koch, P., Zachos, J., and Dettman, D.: Stable isotope stratigraphy and paleoclimatology of the Paleogene Bighorn Basin (Wyoming, USA), *Palaeogeogr. Palaeoclimatol.*, 115, 61-89, [https://doi.org/10.1016/0031-0182\(94\)00107-j](https://doi.org/10.1016/0031-0182(94)00107-j), 1995.
- 650 Konecky, B., Dee, S., and Noone, D.: WaxPSM: A forward model of leaf wax hydrogen isotope ratios to bridge proxy and model estimates of past climate, *Biogeosciences*, 124, 2107-2125, <https://doi.org/10.1029/2018JG004708>, 2019.
- Konecky, B., Noone, D., and Cobb, K.: The influence of competing hydroclimate processes on stable isotope ratios in tropical rainfall, *Geophys. Res. Lett.*, 46, 1622-1633, <https://doi.org/10.1029/2018GL080188>, 2019.
- 655 Lawrence, K., Sloan, L., and Sewall, J.: Terrestrial climatic response to precessional orbital forcing in the Eocene, in: *Causes and Consequences of Globally Warm Climates in the Early Paleogene*, *Geol. Soc. Am.*, 369, <https://doi.org/10.1130/0-8137-2369-8.65>, 2003.
- 660 Lourens, L., Sluijs, A., Zachos, J., Thomas, E., Rohl, U., Bowles, J., and Raffi, I.: Astronomical pacing of late Paleocene to early Eocene global warming events, *Nature*, 435, 1083-1087, <https://doi.org/10.1038/nature03814>, 2005.
- Lunt, D., Ridgwell, A., Sluijs, A., Zachos, J., Hunter, S., and Haywood, A.: A model for orbital pacing of methane hydrate destabilization during the Paleogene, *Nat. Geosci.*, 4, 775-778, <https://doi.org/10.1038/ngeo1266>, 2011.
- 665 Luz, B., Barkan, E., Yam, R., and Shemesh, A.: Fractionation of oxygen and hydrogen isotopes in evaporating water, *Geochim. Cosmochim. Ac.*, 73, 6697-6703, <https://doi.org/10.1016/j.gca.2009.08.008>, 2009.



- 670 Mulch, A., Teyssier, C., Cosca, M., and Chamberlain, C.: Stable isotope paleoaltimetry of Eocene core complexes in the North American Cordillera, *Tectonics*, 26, <https://doi.org/10.1029/2006TC001995>, 2007.
- 675 Muller, R., Cannon, J., Qin, X., Watson, R., Gurnis, M., Williams, S., Pfaffelmoser, T., Seton, M., Russell, S., and Zahirovic, S.: GPlates: Building a virtual earth through deep time, *Geochem. Geophys. Geosy.*, 19, 2243-2261, <https://doi.org/10.1029/2018GC007584>, 2018.
- Pagani, M., Pedentchouk, N., Huber, M., Sluijs, A., Schouten, S., Brinkhuis, H., Damste, J., Dickens, G., and Expedition 302 Scientists: Arctic hydrology during global warming at the Paleocene/Eocene thermal maximum, *Nature*, 442, 671-675, <https://doi.org/10.1038/nature05043>, 2006.
- 680 Poulsen, C. and Jeffery, M.: Climate change imprinting on stable isotopic compositions of high-elevation meteoric water cloaks past surface elevations of major orogens, *Geology*, 39, 595-598, <https://doi.org/10.1130/g32052.1>, 2011.
- Poulsen, C., Pollard, D., and White, T.: General circulation model simulation of the $\delta^{18}\text{O}$ content of continental precipitation in the middle Cretaceous: A model-proxy comparison, *Geology*, 35, 199-202, <https://doi.org/10.1130/g23343a.1>, 2007.
- 685 Rae, J., Zhang, Y., Liu, X., Foster, G., Stoll, H., and Whiteford, R.: Atmospheric CO_2 over the past 66 million years from marine archives, *Annu. Rev. Earth Pl. Sc.*, 49, 609-641, <https://doi.org/10.1146/annurev-earth-082420-063026>, 2021.
- 690 Ruddiman, W.: Orbital changes and climate, *Quaternary Science Reviews*, 25, 3092-3112, <https://doi.org/10.1016/j.quascirev.2006.09.001>, 2006.
- 695 Sachse, D., Billault, I., Bowen, G., Chikaraishi, Y., Dawson, T., Feakins, S., Freeman, K., Magill, C., McInerney, F., van der Meer, M., Polissar, P., Robins, R., Sachs, J., Schmidt, H-L., Sessions, A., White, J., West, J., and Kahmen, A.: Molecular paleohydrology: Interpreting the hydrogen-isotopic composition of lipid biomarkers from photosynthesizing organisms, *Annu. Rev. Earth Pl. Sc.*, 40, 221-249, <https://doi.org/10.1146/annurev-earth-042711-105535>, 2012.
- 700 Singh, H., Bitz, C., Donohoe, A., Nusbaumer, J., and Noone, D.: A mathematical framework for analysis of water tracers. Part II: Understanding large-scale perturbations in the hydrological cycle due to CO_2 doubling, *J. Climate*, 29, 6765-6782, <https://doi.org/10.1175/JCLI-D-16-0293.1>, 2016.



- Smith, F., Wing, S., and Freeman, K.: Magnitude of the carbon isotope excursion at the Paleocene-Eocene thermal maximum: The role of plant community change, *Earth Planet Sc. Lett.*, 262, 50-65, <https://doi.org/10.1016/j.epsl.2007.07.021>, 2007.
- 705
- Snell, K., Thrasher, B., Eiler, J., Koch, P., Sloan, L., and Tabor, N.: Hot summers in the Bighorn Basin during the early Paleogene, *Geology*, 41, 55-58, <https://doi.org/10.1130/g33567.1>, 2012.
- Thompson, A., Zhu, J., Poulsen, C., Tierney, J., and Skinner, C.: Northern hemisphere vegetation change drives a Holocene thermal maximum, *Science*, 8, <https://doi.org/10.1126/sciadv.abj6535>, 2022.
- 710
- Tichy, H., Hellwig, M., and Kallina, W.: Revisiting theories of humidity transduction: A focus on electrophysiological data, *Front. Physiol.*, 8, <https://doi.org/10.3389/fphys.2017.00650>, 2017.
- 715
- Tierney, J., Poulsen, C., Montanez, I., Bhattacharya, T., Feng, R., Ford, H., Honisch, B., Inglis, G., Petersen, S., Sagoo, N., Tabor, C., Thirumalai, K., Zhu, J., Burls, N., Foster, G., Godderis, Y., Huber, B., Ivany, L., Turner, S., Lunt, D., McElwain, J., Mills, B., Otto-Bliesner, B., Ridgwell, A., and Zhang, Y.: Past climates inform our future, *Science*, 370, <https://doi.org/10.1126/science.aay3701>, 2020.
- 720
- Tierney, J., Zhu, J., Li, M., Ridgwell, A., Hakim, G., Poulsen, C., Whiteford, R., Raw, J., and Kump, L.: Spatial patterns of climate change across the Paleocene-Eocene thermal maximum, *P. Natl. Acad. Sci. USA*, 119, <https://doi.org/10.1073/pnas.2205326119>, 2022.
- 725
- Tipple, B., Pagani, M., Krishnan, S., Dirghangi, S., Galeotti, S., Agnini, C., Giusberti, L., and Rio D.: Coupled high-resolution marine and terrestrial records of carbon and hydrologic cycles variations during the Paleocene-Eocene thermal maximum (PETM), *Earth Planet Sc. Lett.*, 311, 82-92, <https://doi.org/10.1016/j.epsl.2011.08.045>, 2011.
- Westerhold, T., Rohl, U., and Laskar, J.: Time scale controversy: Accurate orbital calibration of the early Paleogene, *Geochem. Geophys. Geosy.*, 13, <https://doi.org/10.1029/2012gc004096>, 2012.
- 730
- Westerhold, T., Rohl, U., McCarren, H., and Zachos, J.: Latest on the absolute age of the Paleocene-Eocene thermal maximum (PETM): New insights from exact stratigraphic position of key ash layers +19 and -17, *Earth Planet Sc. Lett.*, 287, 412-419, <https://doi.org/10.1016/j.epsl.2009.08.027>, 2009.



- 735 White, T., Bradley, D., Haeussler, P., and Rowley, D.: Late Paleocene-early Eocene paleosols and a new measure of the transport distance of Alaska's Yakutat terrane, *J. Geol.*, 125, 113-123, <https://doi.org/10.1086/690198>, 2017.
- van Dijk, J., Fernandez, A., Bernasconi, S., Rugenstein, J., Passey, S., and White, T.: Spatial pattern of super-greenhouse warmth controlled by elevated specific humidity, *Nat. Geosci.*, 13, 739-744, <https://doi.org/10.1038/s41561-020-00648-2>,
740 2020.
- van Dijk, J., Fernandez, A., Muller, I., Lever, M., and Bernasconi S.: Oxygen isotope fractionation in the siderite-water system between 8.5 and 62 C, *Geochim. Cosmochim. Ac.*, 220, 535-551, <https://doi.org/10.1016/j.gca.2017.10.009>, 2018.
- 745 van Dijk, J., Fernandez, A., Storch, J., White, T., Lever, M., Muller, I., Bishop, S., Seifert, R., Driese, S., Krylov, A., Ludvigson, G., Turchyn, A., Link, C., Wittkop, C., and Bernasconi, S.: Experimental calibration of clumped isotopes in siderite between 8.5 and 62 C and its application as paleo-thermometer in paleosols, *Geochim. Cosmochim. Ac.*, 254, 1-20, <https://doi.org/10.1016/j.gca.2019.03.018>, 2019.
- 750 Zachos, J., McCarren, H., Murphy, B., Rohl, U., and Westerhold, T.: Tempo and scale of late Paleocene and early Eocene carbon isotope cycles: Implications for the origin of hyperthermals, *Earth and Planet Sc. Lett.*, 299, 242-249, <https://doi.org/10.1016/j.epsl.2010.09.004>, 2010.
- Zeebe, R., Westerhold, T., Littler, K., and Zachos, J.: Orbital forcing of the Paleocene and Eocene carbon cycle,
755 *Palaeoceanography*, 32, 440-465, <https://doi.org/10.1002/2016pa003054>, 2017.
- Zhu, J., Liu, Z., Otto-Bliesner, B., Brady, E., Noone, D., Zhang, J., Tomas, R., Jahn, A., Nusbaumer, J., and Wong, T.: Reduced ENSO variability at the LGM revealed by an isotope-enabled earth system model, *Geophys. Res. Lett.*, 44, 6984-6992, <https://doi.org/10.1002/2017GL073406>, 2017.
- 760 Zhu, J., Poulsen, C., Otto-Bliesner, B., Liu, Z., Brady, E., and Noone, D.: Simulation of Early Eocene water isotopes using an Earth system model and its implication for past climate reconstruction, *Earth Planet Sc. Lett.*, 537, <https://doi.org/10.1016/j.epsl.2020.116164>, 2020.
- Zhu, J., Poulsen, C., and Tierney, J.: Simulation of Eocene extreme warmth and high climate sensitivity through cloud feedbacks, *Science*, 5, <https://doi.org/10.1126/sciadv.aax18>, 2019.

765